RSC Advances

PAPER

View Article Online
View Journal | View Issue

Cite this: *RSC Adv.*, 2026, **16**, 8300

Folic acid-functionalized mesoporous silica nanoparticles integrating fluorouracil-derived carbon dots and porphyrin for targeted breast cancer chemo-photodynamic therapy

Eman Serag,[ab] Esmail M. El-Fakharany,[c] Yousra A. El-Maradny[cd] and Mohamed E. El-Khouly *[a]

We developed herein a new nanoplatform, MSNCDs-FA@TMPyP, for combined chemotherapy and photodynamic cancer therapy. The platform is built on mesoporous silica nanoparticles (MSN) with integrated 5-fluorouracil-derived carbon dots (FU CDs), serving as a dual-function system. Folic acid (FA) was added for targeted delivery to cancer cells, which often have high folate receptor concentrations. Finally, a tetrakis(*N*-methylpyridinium-4-yl) porphyrin (TMPyP) photosensitizer was loaded onto the platform to complete the chemo-photodynamic system. Comprehensive characterization (including TEM, EDX mapping, FTIR, XPS, and UV-vis spectroscopy) confirmed the structure. The synthesized MSNCDs were spherical (100–200 nm), with successful integration of FU CDs into the MSN particles, a finding strongly supported by EDX mapping and XPS. Functionalization with TMPyP and FA was verified by FTIR, Zeta potential, DLS, and UV-vis spectroscopy. The loading capacity of TMPyP is 333.3 mg g^{-1}. For acidic tumour environments, this drug-releasing nanoplatform is pH responsive (89% at pH 5.0, 55% at pH 7.4). Kinetic modelling suggests a synergistic diffusion and matrix erosion process for TMPyP release, with Higuchi (R^2 = 0.99 for pH 5, R^2 = 0.98 for pH 7.4) and Korsmeyer–Peppas mechanisms (R^2 = 0.9696 for pH 5, R^2 = 0.957 for pH 7.4), with release exponents of n = 0.3617 and n = 0.384 for pH 5, 7.4, respectively. The nanoplatform has a selectivity index of 8.44 and a 9-fold increase in cytotoxicity upon light activation for MDA-MB-231 cells. The nanoplatform MSNCDs-FA@TMPyP generated 41.12% early apoptosis, 22.07% late apoptosis, and 5.31% primary necrosis in MDA-MB-231 breast cancer cells upon light activation. This research presents a promising new bifunctional nanocomposite that combines the benefits of targeted chemotherapy and photodynamic therapy, offering a synergistic approach to cancer treatment that could lead to improved outcomes.

Received 27th December 2025
Accepted 22nd January 2026

DOI: 10.1039/d5ra10048h

rsc.li/rsc-advances

Introduction

Traditional cancer treatments, like chemotherapy, often result in unfavorable outcomes due to serious, non-specific side effects on normal tissues and premature drug leakage, which reduces their effectiveness.[1,2] To address these challenges, targeted drug delivery integrates various therapies, including chemotherapy, radiotherapy, and Photodynamic Therapy (PDT).[3] PDT is a promising, minimally invasive treatment alternative to traditional approaches.[4–6] Its innovations include low systemic toxicity and minimal adverse effects,[7] high selectivity and superior therapeutic results, noninvasive administration, faster treatment and suitability for combination therapies, potential to combat bacterial and multidrug resistance, and exploitation of the enhanced permeability and retention (EPR) effect.[8] However, challenges for PDT outcomes still exist, such as issues with biocompatibility, the acidic tumor environment, and complex synthetic methods.[9]

Compared with bulk materials, nanoparticles, such as mesoporous silica nanoparticles (MSNs), are promising tools in cancer therapy due to their large surface area, which allows them to carry multiple therapeutic agents.[8] Recent innovations involve creating multifunctional nanoparticles that combine several treatments into a single platform.[9] For instance, combining carbon dots (CDs) with MSNs has attracted attention because of the unique properties of CDs, but traditional

[a]*Nanoscience Program, Faculty of Basic and Applied Science, Egypt-Japan University of Science and Technology (E-JUST), New Borg El-Arab City, Alexandria 21934, Egypt. E-mail: mohamed.elkhouly@ejust.edu.eg*

[b]*Marine Pollution Department, Environmental Division, National Institute of Oceanography and Fisheries, Kayet Bey, Elanfoushy, Alexandria, Egypt*

[c]*Protein Research Department, Genetic Engineering and Biotechnology Research Institute (GEBRI), City of Scientific Research and Technological Applications (SRTA-City), New Borg El-Arab, Alexandria 21934, Egypt*

[d]*Microbiology and Immunology, Faculty of Pharmacy, Arab Academy for Science, Technology and Maritime Transport (AASTMT), El Alamein 51718, Egypt*

synthesis methods have been complex and inconsistent.[10] To address this, recent research has explored developing more effective nanostructures, such as a core/shell MSN/CD hybrid, for applications like pH-responsive drug release and antibacterial activity.[11–14]

The diminutive size and low density of CDs complicate bulk manufacture, requiring laborious purification and isolation processes. It is essential to synthesize CDs/MSN nanohybrids using a simple one-pot approach. The majority of documented CDs/MSN nanohybrids were produced through a post-synthetic method that proved to be labor-intensive and inconsistent, as the recombination process led to structural changes or damage.[15] The compact dimensions and reduced density of CDs pose challenges for mass production, requiring extensive purification and isolation processes that are time intensive. The development of CDs/MSN nanohybrids through a straightforward one-pot method is essential.[16]

A novel approach entails the incorporation of CDs into the structure of MSNs, yielding unique optical and electrical properties. This research presents a one-pot, efficient synthesis method for generating MSN embedded with carbon dots derived from the chemotherapeutic drug 5-fluorouracil (5-FU). The conversion of 5-FU into carbon dots represents a novel method, in which the chemotherapeutic drug is transformed into fluorescent carbon dots that preserve the therapeutic properties of the original compound. This creates a dual-action treatment platform that combines the cytotoxic effects of chemotherapy with the photodynamic therapy (PDT) properties of carbon dots, while also improving the solubility of silica nanoparticles, hence increasing their bioavailability and therapeutic effectiveness.

The incorporation of 5-FU-derived carbon dots, coupled with the introduction of tetrakis(*N*-methylpyridinium-4-yl)porphyrin photosensitizer (TMPyP), markedly enhances treatment efficacy. TMPyP functions as a potent photosensitiser for photodynamic therapy (PDT), enabling targeted treatment *via* light exposure and inducing cell death through the generation of reactive oxygen species.[17] Nonetheless, its therapeutic utility is frequently constrained by diminished bioavailability and ineffective targeting.[18] Mesoporous silica–carbon dot composites effectively encapsulate TMPyP, improving its stability, solubility, and controlled release to address these problems.[19] The mesoporous architecture enables the encapsulation of TMPyP, whereas the carbon dots enhance photoluminescent imaging capabilities, allowing for real-time monitoring of drug transport and photodynamic therapy.[20]

Moreover, the carbon dots demonstrate potential as a bifunctional medicinal agent. Derived from chemotherapeutic agents, they can operate synergistically with TMPyP to enhance therapeutic outcomes. When derived from chemotherapeutic agents, these CDs can provide additional anticancer effects, facilitating a combination of photodynamic therapy and chemotherapy within a single treatment framework.[21] This dual-action approach enhances the efficacy of cancer treatment while minimizing adverse effects by selectively targeting cancer cells.[22] The integration of chemotherapy and photodynamic therapy (PDT) within a singular nanoparticle system offers a promising solution to the constraints of conventional cancer treatments, enabling a more efficient and focused therapeutic method.[23]

This study seeks to present a novel one-pot production method for MSNs integrated with carbon dots derived from the chemotherapeutic drug 5-fluorouracil (5-FU). This approach seeks to enhance the solubility and therapeutic effectiveness of MSN while enabling a dual-functionality system that combines chemotherapy with photodynamic therapy (PDT) through the integration of TMPyP photosensitizer. Additionally, folic acid (FA) will be conjugated to this platform to enable targeted delivery to cancer cells. The integration of MSN and CDs (MSNCDs) for encapsulating TMPyP photosensitizer presents a promising method to enhance the efficacy of photodynamic therapy, while simultaneously introducing an innovative dual therapy strategy utilizing chemotherapy-derived carbon dots. This composite material shows significant potential for enhancing cancer treatment, providing a more efficient and tailored therapeutic approach.

Materials and methods

Materials

The following chemicals were used: cetyltrimethylammonium bromide (CTAB), tetraethyl orthosilicate (TEOS), *meso*-tetrakis(*N*-methylpyridinium-4-yl) porphyrin tetra(*p*-toluenesulfonate) (TMPyP, purity ≥ 98%), 5-fluorouracil (5-FU, purity ≥ 99%). All compounds were purchased from Sigma-Aldrich, and were used without any further purification. Phosphate buffered saline (PBS, 99%), 1-(3-dimethylaminopropyl)-3-ethylcarbodiimide hydrochloride (EDC, 99.8%), and *N*-hydroxysuccinimide (NHS, 99%) were all obtained from Merk Company. Folic acid (FOLA, 97%) was also purchased from Sigma. Dulbecco's Phosphate-Buffered Saline (DPBS), DMEM and Triton X-100 were obtained from Sigma-Aldrich (USA). The normal human skin fibroblasts line (HSF) was considered a non-cancerous human cell line and three cancerous cell lines from human origins were included: MDA-MB-231 (human breast cancer cell line, epithelial type), HepG2 (human hepatoma-derived cell line) and HCT-116 (human colon cancer cell line) were obtained from American Type Culture Collection (ATCC), Manassas, Virginia, USA. Fetal bovine serum and a sterile Penicillin/Streptomycin solution for cell culture were acquired from BioWest, France. The Apoptosis/Necrosis Detection Kit (BD Pharmingen™ FITC Annexin V Apoptosis Detection Kit I) was supplied by BD Biosciences, Germany. All experiments were conducted using ultrapure water. ELISA kits (ELK Biotechnology, China) specific for human CASP3 (catalog #ELK1527) and CASP9 (catalog #ELK1530) were used for quantifying human caspase-3 and caspase-9 levels according to the manufacturer's instructions (ELK Biotechnology, Wuhan, China). The *in vitro* studying was conducted at the Protein Research Department of the Genetic Engineering and Biotechnology Research Institute (GEBRI) in the City of Scientific Research and Technological Applications (SRTACity), found in New Borg Al-Arab City, Alexandria, Egypt.

One pot step synthesis mesoporous silica nanoparticles/5 fluorouracil carbon dots (MSNCDs). 850 mg of cetyl trimethylammonium bromide (CTAB) and 1 mL of 2.0 M sodium hydroxide were combined with 50 mL of deionized water and stirred for 60 minutes at 95 °C. With vigorous stirring, tetraethyl orthosilicate (TEOS, 1.15 g) was added gradually to the previously mentioned solution. After that, 50 mg of 5-fluorouracil was added, and the mixture was kept at a stirring temperature of 95 °C for an hour. The milk-white slurry was subsequently transferred to a 100 mL autoclave lined with Teflon for hydrothermal treatment at 180 °C for a duration of four hours. The product (MSNCDs) was acquired through centrifugation following rinsing with distilled water and a significant amount of ethanol. The prepared MSNCDs were lyophilized prior to use.[16]

Stability of MSNCDs

Particle size was evaluated using dynamic light scattering (DLS) to measure the size of 1 mg of the synthesized MSNCDs suspended in 5 mL of distilled water over various incubation intervals (0, 24, 72 hours, and 1 week).[24]

Loading of TMPyP on MSNCDs. 10 mg of *meso*-tetrakis (*N*-methylpyridinium-4-yl) porphyrin (TMPyP) was incorporated into an aqueous solution of MSNCDs (24 mg/20 mL dH_2O), and the mixture was agitated overnight. The constructed mechanized nanoparticle was obtained *via* centrifugation (15 000 rpm for 3 minutes), rinsed with distilled water until fluorescence was undetectable, and subsequently dried under vacuum overnight.

Photostability of TMPyP after loading on MSNCDs

The photostability of TMPyP after loading onto MSNCDs was examined by monitoring UV-vis spectra. The samples were subjected to light exposure (xenon arc lamp, Shimadzu RF6000 spectrofluorometer) at time intervals ranging from 0 to 30 minutes. UV-vis spectra were obtained at each time point within the range of 300–700 nm. The absorbance of the Soret band (about 420–430 nm) was observed as a measure of TMPyP stability under light exposure. All studies were conducted at ambient temperature, and measurements were replicated in triplicate to guarantee reproducibility.[25] Moreover, the photostability test was measured in presence of different medium like dH_2O, PBS, and DMEM.

Functionalization of MSNCDs@TMPyP with activated folic acid

To activate the carboxylate group of folic acid, 0.30 g of NHS and 0.15 g of DCC were added to folic acid solution (0.32 g of folic acid in 20 mL of phosphate buffer at pH 7). The mixture was then stirred overnight in the dark. Finally, the material was dried in a vacuum oven at 60 °C for 12 hours.[26]

To functionalize MSNCDs@TMPyP with activated FA in a 2 : 1 ratio. React the mixture in 30 mL of deionized water while stirring vigorously for 72 hours. Afterward, the mixture was subjected to precipitation by centrifugation at 9000 rpm for 20 minutes. The resulting samples were then rinsed twice with a 1 : 1 methanol–water mixture to remove any excess targeting ligands. Finally, the samples MSNCDs-FA@TMPyP were vacuum dried at 60 °C for 12 hours.

Assessment of TMPyP loading and *in vitro* release

The entrapped efficiency obtained by gathering the supernatant to measure the concentration of entrapped TMPyP %.

$$\text{The entrapped efficiency}(\%) = \frac{\text{drug}_{\text{total}} - \text{drug}_{\text{unloaded}}}{\text{drug}_{\text{total}}} \times 100 \quad (1)$$

The term "Drug Total" refers to the initial weight of the photosensitizer P_s before it is loaded onto the carrier. On the other hand, "Drug unloaded" refers to the weight of the free P_s in the supernatant.[27]

In vitro experiments on TMPyP release were conducted in PBS at varying pH levels (pH 5 and 7.4) using dialysis bag diffusion. A TMPyP-loaded sample (2 mg) was dispersed in 2 mL of PBS buffer and subsequently, transferred to a dialysis bag (3 KDa) for release into 20 mL of PBS. At selected time intervals, 2 mL of supernatant was extracted, and the concentration of TMPyP was measured using UV-vis absorbance at 420 nm. An equal volume of fresh PBS at varying pH levels was added to maintain the total volume.

The data were analyzed using a variety of models, such as the Korsmeyer and Peppas model, Higuchi's diffusion control model, first order, and zero order, to investigate the release mechanism of TMPyP from MSNCDs-FA@TMPyP. We provide the equations for each model in the SI (S1) and present the TMPyP calibration curve in Fig. S1.

Characterization techniques. The size and shape of the prepared MSNCDs were investigated by transmission electron microscopy (TEM) using a JEOL 2100 PLUS, Japan, ImageJ software was used to determine the particle size distribution of all samples (TEM images), for each sample more than 100 particles were measured. The prepared materials were also studied by X-ray diffraction (XRD) using a The X-ray 7000 Shimadzu, Japan. The experimental conditions are Bragg angle (2θ) within the range of 10 to 80°, with Cu-Kα radiation ($\lambda = 1.5405$ Å), an operating voltage of 30 kV and current of 10 mA. The elemental composition of the synthesized materials was determined by X-ray photoelectron analyzer (K-alpha+, ThermoFisher Scientific, Waltham, MA, USA). The functional groups on the materials were recorded using Fourier-Transform Infrared (FT-IR) spectra using an IRAffinity-1 spectrometer (Shimadzu, Japan). UV-vis absorption measurements were performed with a UV-2350 spectrophotometer (Shimadzu, Japan). Photoluminescence properties were investigated using an RF-5301 fluorescence spectrometer (Shimadzu, Japan). The measurement of particle size distribution for prepared materials was conducted through dynamic light scattering (DLS) utilizing Nano-ZS (Malvern Instruments, UK).

Photodynamic procedure: cells were illuminated with a light-emitting diode (LED) array at 420 nm (power density = 1.5 mW cm^{-2}, irradiation time 15 min). The LED array was positioned at

a consistent distance to maintain uniform exposure. The cumulative light dosage delivered during photodynamic procedure was calculated as the following: the light dose = 1.5 × 10^{-3}W cm^{-2} × 900 s = 1.35 J cm^{-2}. This condition falls within the normal range of light doses currently reported for *in vitro* PDT investigations (1–50 J cm^{-2}). And selected based on a previous study to ensure effective TMPyP activation with a minimum thermal effect.[28,29]

Extracellular $^{\cdot}$OH detection (methylene blue degradation by $^{\cdot}$OH). 1 mg of MSNCDs, and MSNCDs-FA@TMPyP was mixed with 5 mL of a solution of methylene blue (MB) that had 20 mM hydrogen peroxide (H_2O_2). After being exposed to radiation (1.5 mW cm^{-2} LED, 420 nm), the MB solution was spun to get rid of the MSN CDs NPs. A UV-vis spectrophotometer was then used to measure the absorbance at 664 nm. For comparison, a similar experiment was done without light or H_2O_2 to see how the MB would break down in those situations.[30]

Hemolysis test. The human red blood cells used for the hemolysis assay were obtained from a licensed clinical laboratory (Alpha Lab, Alexandria, Egypt). The blood samples were collected from healthy adult donors following the routine procedures and ethical guidelines.

The blood sample was centrifuged at 2000 rpm for 5 minutes to remove the supernatant. The red blood cells were washed three times with PBS and subsequently diluted in a 1 : 10 ratio with PBS. The synthesized nanomaterials (MSNCDs and MSNCDs-FA@TMPyP) were added to 100 μL of the red blood cell suspension to achieve concentrations of 20, 40, 80, 120, and 160 μg mL^{-1}. The solution's total volume was 2 mL. The negative control group utilized red blood cells combined PBS for 0% hemolysis, while the positive group employed red blood cells mixed with 0.5% (wt) Triton X-100 for 100% hemolysis. The tubes were centrifuged at 2000 rpm for 5 minutes following a 2-hour incubation at 37 °C for picture capture. Readings from the spectrophotometer were obtained for the resulting supernatant at a wavelength of 450 nm.[31] The hemolysis rate was calculated using the following equation:

$$\text{Hemolysis rate } \% = \frac{A_t - A_{neg}}{A_{pos} - A_{neg}} \times 100$$

A_t the absorbance of the test sample, A_{neg} and A_{pos} represent negative and positive control, respectively.

Assessment of *in vitro* cytotoxic effects

The cytotoxic effects of the compounds were evaluated through *vitro* cell culture assays. This evaluation focused on four specific cell lines: the normal human skin fibroblast line (HSF) and three cancerous lines: MDA-MB-231 (epithelial, human breast cancer cell line), HepG-2 (human hepatoma-derived cell line), and HCT-116 (human colon cancer cell line). The research aimed to assess cytotoxicity in both standard (dark) and light-activated conditions, utilizing the Thiazolyl Blue Tetrazolium Bromide (MTT) assay as previously outlined.[32]

Cell lines were maintained in culture using Dulbecco's Modified Eagle Medium (DMEM) supplemented with 10% (v/v) fetal bovine serum (FBS), 1% (v/v) penicillin–streptomycin solution (100 U mL^{-1} penicillin and 100 μg mL^{-1} streptomycin), and 1% L-glutamine. Cell lines were incubated at 37 °C in a humidified incubator with 5% CO_2. Media was replaced every 2–3 days, and cells were passaged using 0.25% trypsin-EDTA solution upon reaching approximately 80% confluence.

Following this, the cells were exposed to the synthesized compounds, diluted to final concentrations between 25 and 800 μg mL^{-1}. HSF and MDA-MB-231 cells were cultured in DMEM, whereas HepG-2 and HCT-116 cells were maintained in RPMI-1640 medium, with each well containing a total volume of 200 μL. The initial assessments of cytotoxicity were conducted without light exposure. In a parallel experiment aimed at assessing photodynamic activity, all cell lines were subjected to the compounds within a lower concentration range of 1.5 to 48.0 μg mL^{-1}. The plates underwent laser irradiation at a wavelength of 420 nm and a power density of 1.5 mW cm^{-2} for 15 minutes.

After a 48-hour incubation period under standard conditions, the culture medium was aspirated, and the cells were washed three times with phosphate-buffered saline (PBS) to eliminate cellular debris and unattached, non-viable cells. Subsequently, 200 μL of a 0.5 mg mL^{-1} MTT solution was introduced to each well. The plates were agitated at 150 rpm for five minutes and subsequently returned to the incubator for 2 to 4 hours, enabling viable cells to metabolize the MTT into formazan crystals. After this metabolic conversion, the MTT-containing medium was removed. To solubilize the formazan crystals, 200 μL of dimethyl sulfoxide (DMSO) was added to each well, followed by an additional five-minute agitation period. Absorbance, which reflects the quantity of formazan produced and indicates cell viability, was measured spectrophotometrically at 570 nm.

The percentage of viable cells was calculated using the formula:

$$\text{Relative cell viability } (\%) = \frac{\text{Mean absorbance of the treated sample}}{\text{Mean absorbance of the untreated control}} \times 100$$

The half-maximal inhibitory concentration (IC_{50}) values, which represent the concentration required to inhibit 50% of cell growth, were calculated by plotting the concentration–response curves using GraphPad Prism software (version 8.0).

To determine the cancer-specific toxicity, a selectivity index (SI) was determined by calculating the ratio of the IC_{50} value against the normal HSF cell line to the IC_{50} value against each cancer cell line. Furthermore, to visually confirm the cytotoxic effects, the morphological changes in the MDA-MB-231 cell line were observed and documented using an inverted phase-contrast microscope (Olympus, Germany) after treatment with IC_{50} concentrations of the compounds, under both dark and light conditions. All experiments were performed in triplicate, with untreated cells as the negative control and 5-fluorouracil-treated cells as the standard treatment.

Quantification of intracellular reactive oxygen species (ROS)

The capacity of the tested compounds to induce oxidative stress was investigated by measuring the generation of intracellular reactive oxygen species (ROS) within the MDA-MB-231 cells. This was achieved using the fluorescent probe 2′,7′-dichlorodihydrofluorescein diacetate (DCFH-DA), following established protocols.[29] Briefly, MDA-MB-231 cells were treated with compounds for 48 hours under both light and dark conditions. Following this treatment period, the intracellular ROS levels in both the treated and untreated control cells were quantified. The generation of ROS, indicated by the fluorescence of the oxidized probe, was visualized and captured using fluorescence microscopy (Olympus, Germany), providing qualitative evidence of oxidative stress induction.

Flow cytometric analysis

Adherent MDA-MB-231 cells were first detached using trypsin, washed with PBS, and then fixed in cold 70% ethanol overnight at 4 °C. The fixed cells were subsequently stained for 2 hours at 4 °C in a PBS-based buffer containing 50 μg mL^{-1} PI and 20 μg mL^{-1} RNase. The Annexin V-FITC/PI-stained cells method was used to investigate the apoptotic and necrotic processes of the modified MSNCDs-FA@TMPyP compound in MDA-MB-231 cells under both light and dark conditions. The apoptotic cell population was measured using the Annexin V-FITC signal detector. Necrotic cells were detected using the propidium iodide (PI) emission signal detector. Data acquisition and analysis were performed on a BD FACSCalibur flow cytometer (BD Biosciences, Heidelberg, Germany) using FlowJo 10.0.7 software (Treestar Inc., Ashland, US).

Caspase activity assay

The activity of caspase-3 and caspase-9 was quantified using commercially available colorimetric ELISA kits (ELK Biotechnology, China) specific for human CASP3 (catalog #ELK1527) and CASP9 (catalog #ELK1530). Following the manufacturer's protocol, cell lysates from treated MDA-MB-231 cells were analyzed. The resulting color development, which is proportional to caspase activity, was measured by reading the absorbance at 450 nm using an ELISA microplate reader.

Statistical analysis

Experiments were performed in triplicate wells and repeated three independent times. Data are presented as the mean ± standard deviation (SD) of the three independent experiments. Statistical analysis was performed using one-way analysis of variance (ANOVA) to determine differences among groups, utilizing SPSS and GraphPad Prism version 8 software. A p-value < 0.05 was considered statistically significant.

Results and discussion

Our work shows that mesoporous silica nanoparticles may be successfully synthesized using a sol–gel reaction, which incorporates 5-fluorouracil, a chemotherapeutic drug, straight into the reaction mixture. The drug was then transformed into carbon dots for the first time using a unique hydrothermal carbonization technique. This method allows for dual functionality and improves cellular uptake. After that, the nanoplatform was coupled with folic acid to improve selectivity for cancer cells and loaded with the photosensitizer TMPyP to promote a synergistic photodynamic treatment (PDT) effect (Scheme 1).

Fig. 1A–D depicted the morphology of MSNCDs. The synthesized mesoporous silica *via* sol–gel reaction has spherical shape and uniform distribution. The particle size range from 100 to 200 nm, which consistent with the pervious findings.[33] the dark spots or dots on or around silica surface indicate the incorporation of carbon dots into mesoporous silica. The

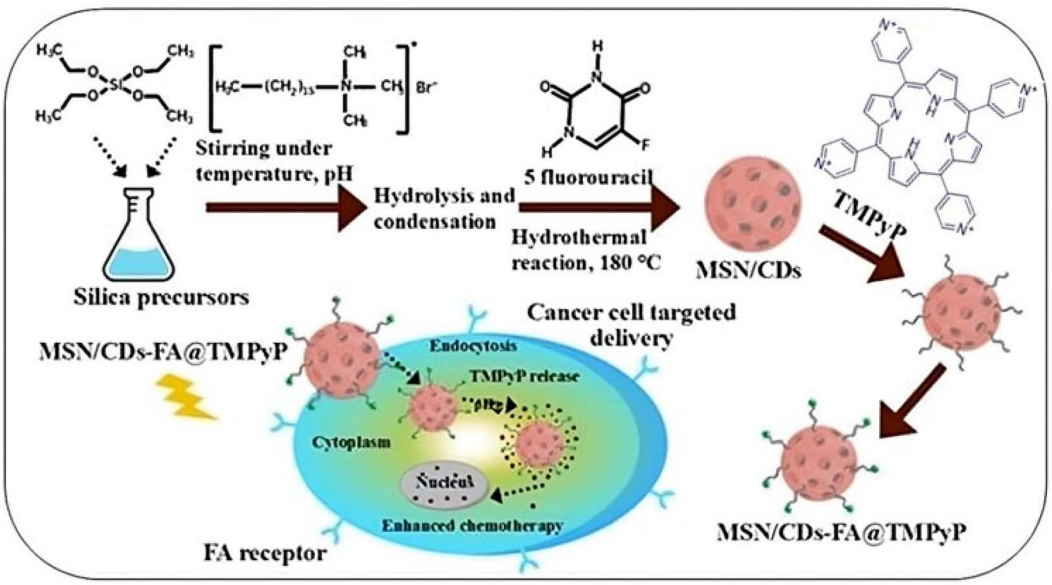

Scheme 1 One simple synthesis of mesoporous silica incorporated fluorouracil carbon dots for synergetic effect on cancer cells.

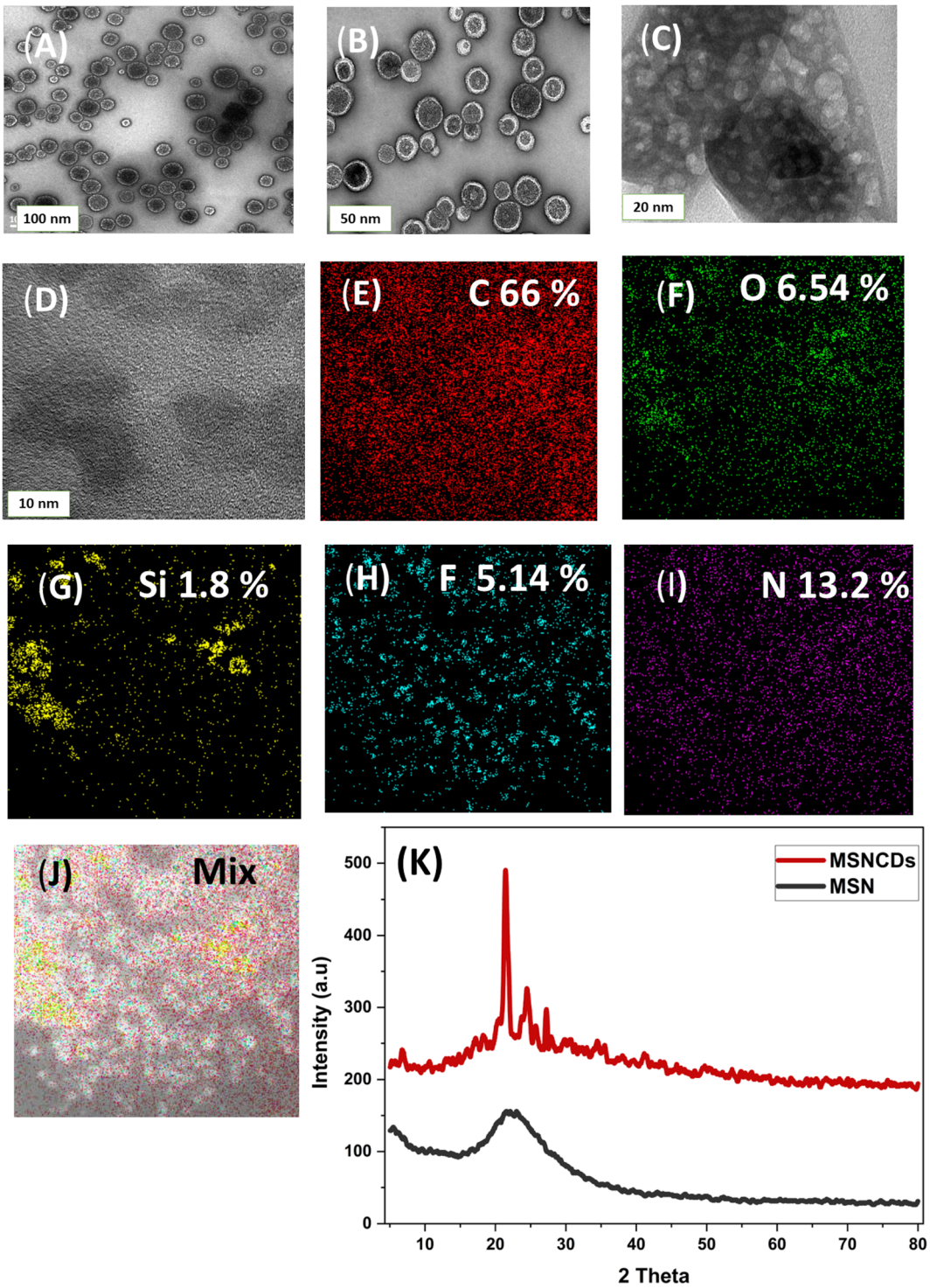

Fig. 1 (A–D) TEM images, (E–J) represent EDX map of the synthesized MSNCDs. (K) X-ray diffraction (XRD) patterns of the synthesized MSNCDs compared with pristine mesoporous silica nanoparticles (MSN) without carbon dots.

uniform distribution of carbon dots, devoid of aggregation, indicates a robust interaction with silica pores. The TEM results validate the effective synthesis of a mesoporous silica–carbon dot composite, with carbon dots integrated within the mesoporous channels.

Fig. 1E–J demonstrated the elemental composition of MSNCDs was analyzed by energy-dispersive X-ray spectroscopy (EDX) mapping. The EDX map verified the successful integration of 5-fluorouracil-derived carbon dots (5FUCDs) with the MSN. The elemental analysis indicated the presence of silicon (Si) and oxygen (O), consistent with the structure of mesoporous silica. Signs of carbon (C), nitrogen (N), and fluorine (F) were also present.

The presence of carbon, nitrogen, and fluorine within the MSN matrix confirms the proper dispersion and integration of 5-FU CDs into or onto the MSN. Carbon and nitrogen are attributed to the organic components of carbon dots, while the fluorine atom is characteristic of 5-fluorouracil, the source of carbon dots. This confirms that the chemical structure of 5-fluorouracil as a precursor persists after carbonization.

The X-ray diffraction (XRD) patterns elucidate the structural properties of both pure silica nanoparticles (MSN) and carbon dot-embedded silica (MSNCDs) composites (Fig. 1K). A broad diffraction peak centered at $2\theta \approx 25°$ was observed for pure silica nanoparticles. This expansiveness is indicative of amorphous silica, which is devoid of long-range crystallinity. The outcome aligns with literature findings regarding colloidal or mesoporous silica, wherein the disordered Si–O–Si network results in diffuse scattering instead of distinct Bragg reflections.[34]

A significant alteration in the XRD pattern was observed following the incorporation of carbon dots (CDs) into the silica matrix *via* a one-step hydrothermal synthesis. The former broad peak became markedly sharper and more intense in the same 2θ region. This phenomenon can be ascribed to the inclusion of graphitic carbon structures from the CDs, which generally display a diffraction peak near $2\theta = 24–26°$, corresponding to the (002) plane of graphitic carbon. The acuity of this peak indicates a greater level of organization within the carbonaceous domains, likely attributable to π–π stacking interactions among the carbon layers.[35]

Moreover, hydrothermal treatment may have caused localized structural reorganization within the silica matrix, facilitating short-range order or partial condensation of silanol groups, thus improving the overall structural clarity observed in XRD. The findings indicate the successful incorporation of carbon dots into the silica matrix, resulting in a hybrid nanocomposite with potentially modified physicochemical characteristics. The improved ordering observed in the XRD pattern corroborates the development of core–shell or uniformly distributed CD structures within the silica matrix, potentially affecting the material's optical, electronic, or drug-loading properties.

X-ray photoelectron spectroscopy (XPS) was employed to examine the surface chemical composition of the synthesized MSNCDs (Fig. 2). The survey spectrum validated the presence of silicon (Si), oxygen (O), carbon (C), nitrogen (N), and fluorine (F), which demonstrate effective functionalization. A significant Si 2p signal observed around 103 eV corresponds to the Si–O bonds within the silica nanoparticle core.[36] The O 1s peak detected around 531–533 eV indicates contributions from Si–O–Si structures as well as oxygen-containing functional groups such as C=O and C–O, which are derived from fluorouracil carbon dots.[16] The C 1s spectrum displayed several components: C–C/C=C (~284.6 eV), C–N/C–O (~286 eV), and C=O (~288 eV), thereby confirming the intricate organic environment present on the nanoparticle surface.[37] The detection of N 1s at approximately 399 eV and F 1s at around 687 eV confirms the incorporation of fluorouracil, as these signals are indicative of its pyrimidine ring and C–F bond, respectively.[38,39] The results confirm the successful integration of fluorouracil-derived carbon dots onto the silica nanoparticle surface, consistent with the EDX findings, thereby supporting their potential application in drug delivery and theragnostics.

Fourier-transform infrared (FTIR) spectroscopy was performed to confirm the result of XPS about the functional groups of the synthesized nanomaterials and the successful loading of TMPyP. The FTIR spectrum exhibited several characteristic peaks that reflect the successful integration of 5-FU CDs into the MSN (Fig. 3A). The broad band appear at 1000 cm^{-1} corresponding to vibrational of Si–O–Si bonds, which is typical for mesoporous silica network.[40] While the spectra at 1200 cm^{-1} is attributed to symmetric Si–O stretching or Si–OH bending, which also confirm the presence of the silica framework.[41] Otherwise, the bands at 1500 cm^{-1} and 2200 cm^{-1} attributed to carbon–carbon (C=C) and possibly carbon–nitrogen (C≡N or C=N) related to functional groups introduced by the 5-FU-derived carbon dots.[42] These peaks associated to sp^2 hybridized carbon structures and nitrogen-containing heterocycles, which are known to remain partially intact during the carbonization of nitrogen-rich precursors like 5-fluorouracil. The weak absorption band observed near 2700 cm^{-1} is attributed to C–H stretching vibrations. These vibrations typically arise from $–CH_2$ or $–CH_3$ groups either on the surface of the carbon dots (CDs) or from residual organic groups within the silica matrix.[43]

Additionally, a prominent signal centered at 3000 cm^{-1} is ascribed to the O–H stretching vibration, signifying the existence of surface hydroxyl groups.[42] These may originate from residual silanol (Si–OH) groups on the silica surface and hydroxyl groups on the carbon dots, enhancing the hydrophilic characteristics and possibility for additional surface functionalization of the hybrid material.[44] The spectra of the silica–carbon dots composite confirm the successful integration of the inorganic (Si–O–Si) and organic (C–C, C–N, O–H) components. The presence of these surface functional groups enhances the loading of therapeutic medicines and facilitates conjugation with targeted ligands.[45]

Alternatively, a notable series of bands detected following the loading of TMPyP. The significant characteristic is the band around 1050 cm^{-1}, ascribed to $C–N^+$ stretching, which serves as a diagnostic indicator of the quaternized nitrogen atoms in the *N*-methylpyridinium groups.[44] Characteristic C–H out-of-plane bending vibrations are seen in the 850–750 cm^{-1} region. These signify the para-substituted characteristics of the pyridyl groups at the meso-positions of the porphyrin ring.[46] Furthermore, the appearance of porphyrin ring skeletal bending vibrations in the 700–650 cm^{-1} range confirms the successful incorporation of TMPyP, either on the MSNCD surface or within its mesoporous framework.[47]

UV-vis spectroscopy was utilized to observe the incremental functionalization of silica nanoparticles containing fluorouracil–carbon dots (MSNCDs), subsequently followed by the incorporation of the porphyrin derivative TMPyP and conjugation with folic acid (Fig. 3B). The initial UV-vis spectra of fluorouracil-derived carbon dots display a characteristic peak at 260 nm, indicative of $\pi \rightarrow \pi^*$ transitions in the uracil ring,[48] confirming that fluorouracil remains chemically stable

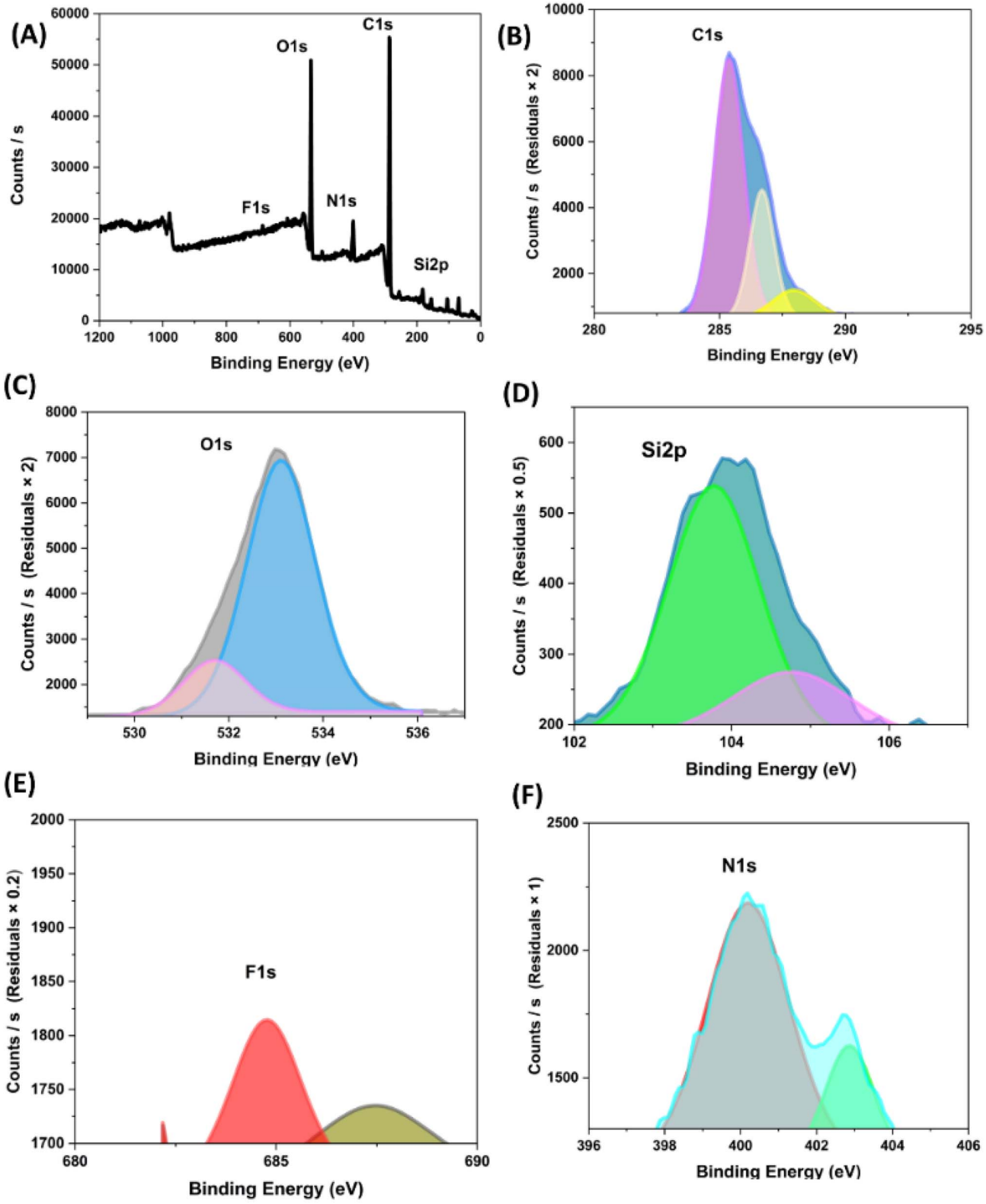

Fig. 2 PS survey spectrum of the synthesized MSNCDs (A) and high-resolution XPS spectra (B–F) of carbon (C), oxygen (O), silicon (Si), fluorine (F), and nitrogen (N).

following its conversion into carbon dots. MSNCDs displayed two different distinctive absorption peaks, with the peak at 260 nm confirming the integration of mesoporous silica and FU-derived carbon dots. The peak at 420 nm displays $n \rightarrow \pi^*$ transitions resulting from the interaction between 5-Fu and silanol groups or residual surface functionalities.[49]

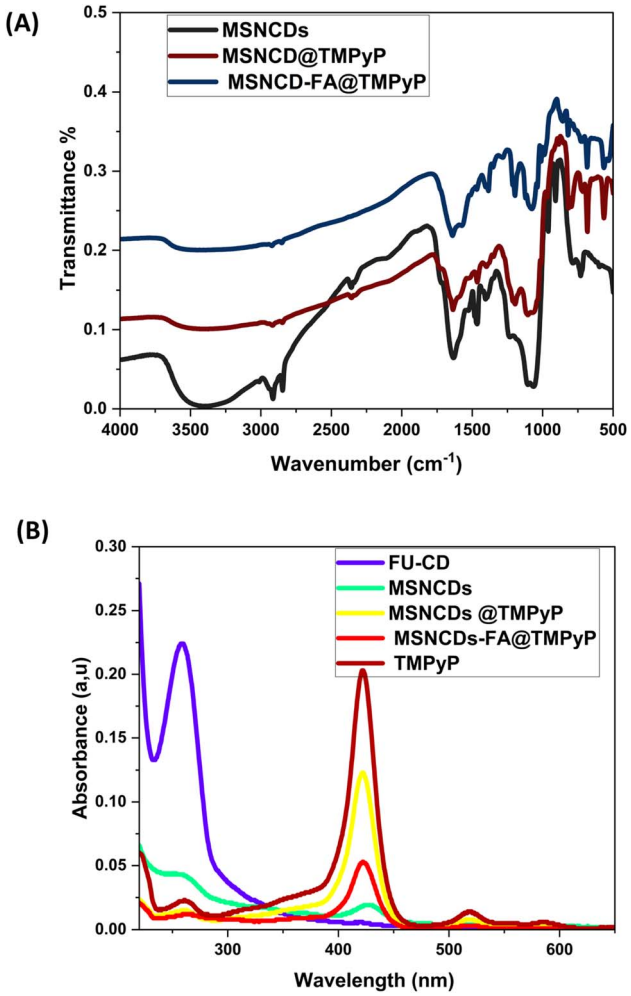

Fig. 3 (A) FTIR spectra, (B) UV-vis analysis of the synthesized MSNCDs, MSNCDs@TMPyP, and MSNCDs-FA @TMPyP.

Upon the introduction of TMPyP, the spectra exhibited a distinct Soret band in the range of 420–430 nm, accompanied by subdued Q-bands within the 500–700 nm region—attributes typical of porphyrin compounds.[50] This validated the effective integration of TMPyP into the nanoparticle system. Significantly, after conjugation with folic acid, the intensity of the porphyrin peaks diminished, indicating a modification in the immediate environment or potential quenching effects. This decrease may be ascribed to steric hindrance or electronic interactions between folic acid and the TMPyP moieties, potentially modifying the porphyrin aggregation state or microenvironment. The spectrum alterations unequivocally demonstrate effective successive functionalization and imply that the ultimate folate-conjugated system preserves the porphyrin chromophores while incorporating targeting functionality through folic acid.[51,52]

Photostability is crucial for evaluating photosensitizers in practical applications, especially in photodynamic treatment. In most dye-based photodynamic therapy systems, the efficacy of photosensitizers may be influenced by nonspecific surface adsorption, aggregation tendencies, and photobleaching. The encapsulation of dye within a host environment inhibits aggregation interactions and non-radiative routes. The photostability of TMPyP was examined in the presence of MSNCDs encapsulation and compared with free TMPyP under low irradiance light from a xenon arc lamp (Shimadzu RF6000 spectrofluorometer) for 30 minutes at 422 ± 2.5 nm. The absorption spectra and the corresponding plots of absorbance at the Soret band (422 nm) over irradiation time (Fig. S2A–D) demonstrate that encapsulation in MSNCDs significantly enhances the photostability of TMPyP. The figure demonstrates that MSNCDs offers a physical barrier that diminishes TMPyP's direct exposure to environmental elements such as oxygen, moisture, and light, which are significant contributors to photodegradation. When TMPyP is encapsulated or adsorbed within the mesopores of silica, it is partially shielded from direct irradiation, resulting in less photobleaching. It also restricts TMPyP's structural alterations or self-aggregation that expedite photodegradation.

The photostability of TMPyP and MSNCDs-FA@TMPyP was evaluated *via* UV-vis absorption spectra in various media, including dH_2O, PBS, and DMEM (Fig. S3). The finding indicated that the stability of free TMPyP and the nanohybrid MSNCDs-FA@TMPyP was optimum in dH_2O, moderate in DMEM, and minimum stability in PBS. The high stability of TMPyP and the nanohybrid in dH_2O is attributed to the lack of salt and proteins, reducing the likelihood of aggregation and breakdown. While PBS's low stability is probably because to its high ionic strength and phosphate ions, which might cause TMPyP to aggregate, change its electrical environment, or interfere with its surface interaction with the nanocarrier.[53] Otherwise, degree of interaction with amino acids, proteins, or salts in DMEM, potentially undermining stability.[54] Overall stability in physiological conditions is critical to preserve the structural integrity and photophysical characteristics of TMPyP-based systems, and emphasis that the composition of the medium is critical for biomedical applications.

Dynamic light scattering (DLS) and zeta potential studies were conducted (Fig. 4) to further elucidate the physicochemical alterations after the sequential functionalization of the MSNCDs composite with TMPyP and FA. The hydrodynamic diameter of the initial MSNCDs material was around 182 nm, exceeding the average particle size observed in TEM images. This attributed by that DLS quantifies the hydrodynamic diameter, surrounding not only the core particle size but also surface-bound molecules and the solvation layer in aqueous suspension.[55] Following the incorporation of the cationic photosensitizer TMPyP, the hydrodynamic size increased to 421 nm, showing good loading of TMPyP onto the surface of silica–carbon dots or within the porous structure of silica nanoparticles. After conjugation with folic acid, the particle size rose to 498 nm, indicating effective surface functionalization with FA. The gradual enlargement during the functionalization stages verifies the incremental alteration of the particle surface and affirms the structural integrity of the core material throughout the modification procedure.[56]

Despite the hydrodynamic diameter (measured by DLS) exceeding 100 nm, the material remains relevant for biomedical

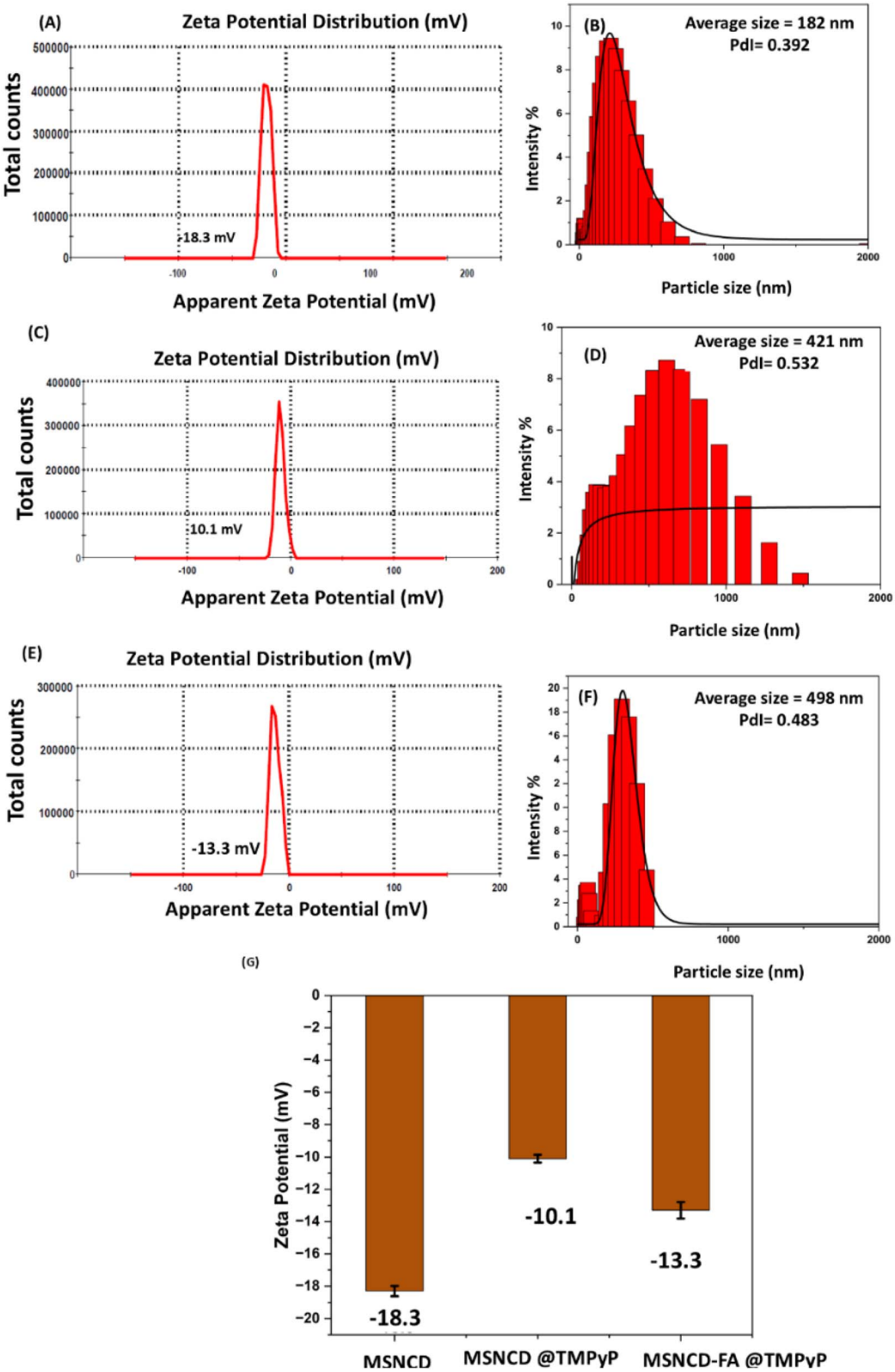

Fig. 4 Zeta potential of (A) MSNCDs, (C) MSNCDs@TMPyP, (E) MSNCDs-FA@TMPyP. Dynamic Light Scattering (DLS) of (B) MSNCDs, (D) MSNCDs @TMPyP, (F) MSNCDs-FA@TMPyP, and (G) the values of zeta potential of the synthesized nanocomposites.

applications as a nanomaterial. Previous studies show that the optimal hydrodynamic size for efficient cellular uptake, prolonged circulation time, and tumor accumulation *via* the Enhanced Permeability and Retention (EPR) effect typically falls between 100–500 nm.[57–61] The DLS-generated hydrodynamic diameter represents an apparent size, which includes the

inorganic core, organic layers, the hydration shell, and potential aggregation in suspension. Conversely, Transmission Electron Microscopy (TEM) confirmed that the core sizes were under 100 nm, validating the nanoscale nature of the MSNCDs-based delivery platform. Therefore, even with a larger hydrodynamic size, the composite fits the definition of a nanoparticle-based delivery platform accepted in nanomedicine.

The zeta potential was examined to corroborate the findings of FTIR and DLS about the functionalization process (Fig. 4). The zeta potential of the initial mesoporous silica–carbon dot system was measured at −18.3 mV, indicating a moderately negative value, which is ascribed to the presence of silanol groups in silica and the functional groups in carbon dots.[62] Upon loading TMPyP, the zeta potential shifted to −10.1 mV, signifying a partial neutralization of the surface charge resulting from the interaction between cationic TMPyP molecules and the negatively charged MSNCD surface.[63] Following the conjugation of folic acid, the zeta potential exhibited a little reduction to −13.0 mV. This may be due to the presence of supplementary carboxylic acid or hydroxyl groups from folic acid, which partially reinstates the negative surface charge.[64] The consistently moderate negative zeta potential at all stages indicates favorable stability in aquatic environments, advantageous for biological applications. Conversely, DLS for MSNCDs at the specified period was examined to verify the aqueous stability of MSNCDs (Fig. 4).

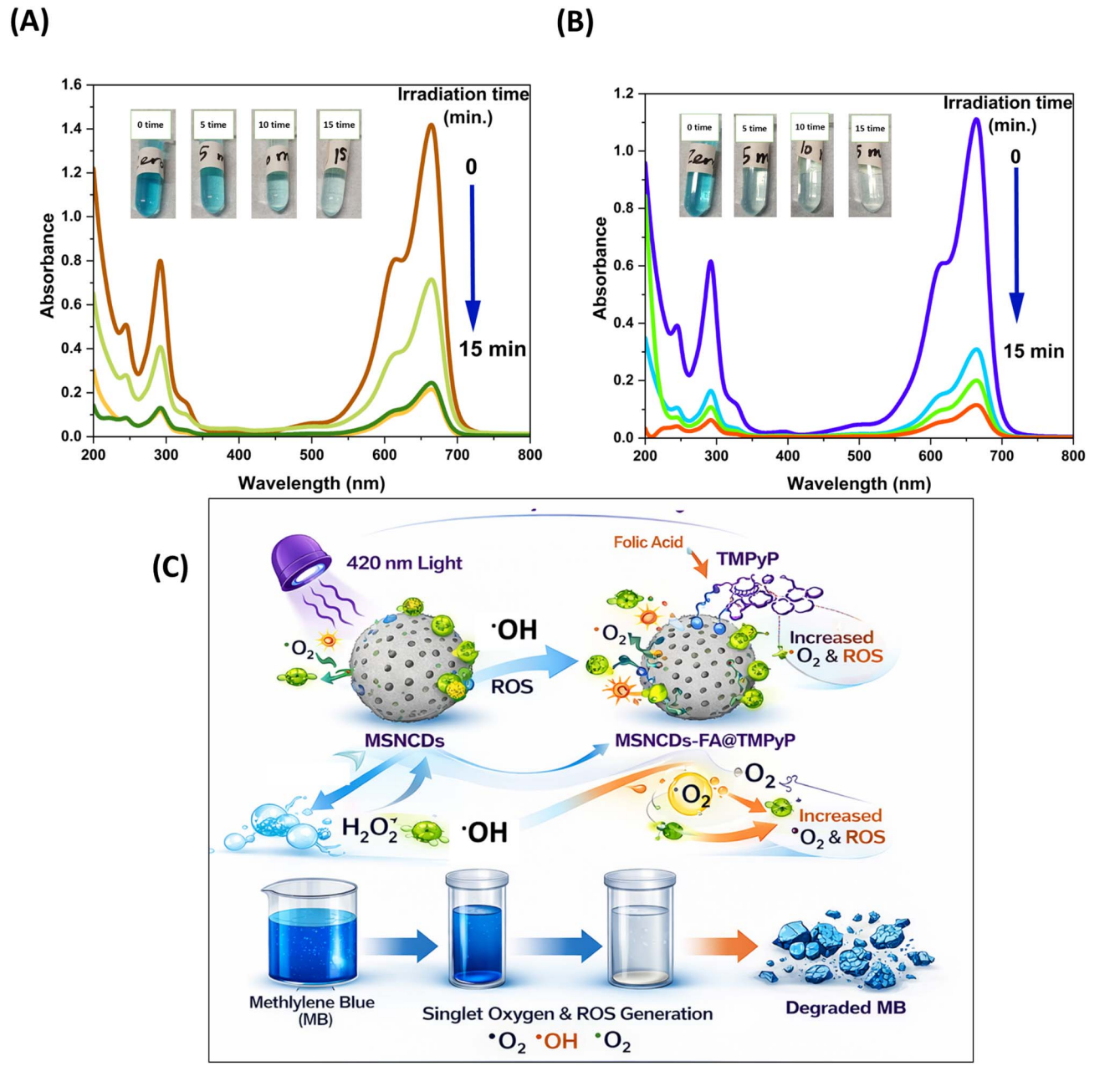

Fig. 5 Methylene blue degradation in prescence of (A) MSCNDs, (B) MSNCDs-FA@TMPyP. The inset represents the photographic images of the samples at different time irradiation. (c) Illustration diagram of MB degradation mechanism in the presence of the synthesized materials.

DLS measurements performed over seven days confirm the colloidal stability of the MSNCDs NPs (Fig. S4). Initially, MSNCDs exhibited a hydrodynamic diameter of 182 nm *via* DLS, indicating excellent dispersion in aqueous solution. On the other hand, DLS after 24 h was 198 nm, and after 72 h was 216 nm while after 1 week the dispersion MSNCD was 220 nm. The finding suggests mild aggregation and slight structural rearrangement, and the minor change in DLS exhibits acceptable colloidal stability over the extended time (1 week) which support the potential of MSNCDs as nanocarrier for medical application.

Extracellular $^{\cdot}OH$ detection (methylene blue degradation)

MB degradation following the exposure to light at (420 nm, 1.5 mW cm^{-2}) in the presence of 20 mM H_2O_2, MSNCDs, and MSNCDs-FA@TMPyP at time interval 0, 5, 10, and 15 minutes was illustrated in Fig. 5. The photoreactivity of the carbon dots within the MSNCDs led to the significant degradation of MB. This activity is attributed to the presence of heteroatoms and surface defects, which facilitate the generation of reactive oxygen species (ROS) under light irradiation.[65] A significant two-fold increase in MB degradation was observed upon loading TMPyP onto the MSNCDs. As a cationic porphyrin, TMPyP generates singlet oxygen and other ROS upon light activation; this introduces a secondary reactive species generation mechanism that enhances the overall photoactive performance of the nanoplatform.[66]

Similarly consistent with the previously described literature, the fluorescence properties of carbon nanodots prepared in different reaction conditions varied significantly. For instance, carbon nanodots solvothermally synthesized in formamide solution showed blue fluorescence and could produce multiple reactive oxygen species, such as hydroxyl radicals (^{-}OH), superoxide anions ($^{-}O_{2-}$), as well as singlet oxygen ($^{1}O_2$), thereby acting as both Type I and Type II photosensitizers.[67] On the contrary, carbon nanodots synthesized in aqueous solutions showed green fluorescence and only produced singlet oxygen species; thus, the photosensitization process followed the Type II mechanism. Three kinds of RCDs that have maximum emission around 680 nm were obtained successfully. These RCDs have controllable ROS production, and the evidence points towards equal contributions from type I photoreactions, which involve the formation of a superoxide anion, and an increasing trend for type II photoreactions, which involve the formation of singlet oxygen.[68]

TMPyP loading and releasing properties

The loading capacity and efficiency of TMPyP were evaluated to assess the performance of MSNCDs. A high loading efficiency of 80% confirms that most of the TMPyP was successfully integrated into the matrix. This high uptake is attributed to a combination of the mesoporous structure, electrostatic interactions, π–π stacking, and physical adsorption. The results revealed a loading capacity of 333.3 mg g^{-1}, a significant value for medicinal applications. This high loading efficiency facilitates effective drug delivery while minimizing the required carrier dose, potentially enhancing therapeutic efficacy while reducing systemic toxicity.

The release profile of TMPyP exhibited a clear pH-responsive behavior, as illustrated in Fig. S5. The cumulative release of TMPyP was significantly higher at pH 5.0 (89%) compared to physiological pH 7.4 (55%). This accelerated release under acidic conditions is attributed to the protonation of functional groups within the MSNCD matrix, which weakens the electrostatic and hydrogen bonding interactions between the drug and carrier. Furthermore, at lower pH, the enhanced solubility of TMPyP and potential structural changes in the nanocarrier facilitate increased drug diffusion from the mesoporous channels.

At pH 7.4, the enhanced interactions between the neutral or negatively charged matrix and the cationic TMPyP likely impede the release process. The pH-sensitive release profile is beneficial for targeted cancer therapy, facilitating efficient drug release in the acidic tumor microenvironment or intracellular compartments like lysosomes, while ensuring controlled release under normal physiological conditions to minimize off-target effects.[68,69]

Kinetic analysis of TMPyP release from the MSNCDs indicates that the data align most closely with the Higuchi and Korsmeyer–Peppas models. These models yielded superior R^2 values compared to the zero-order, first-order, and Hixon–Crowell models, as summarized in Table 1 and Fig. S5. The Higuchi model showed a strong correlation with the release data (R^2 = 0.99 for pH 5.0 and R^2 = 0.98 for pH 7.4), confirming that the

Table 1 Mathematical models (zero order, first order, Higuchi, Korsmeyer–Peppas, and Hixon–Crowell) and different kinetics parameters of TMPyP release from MSNCDs-FA at pH 5, and pH 7.4

Kinetic model	Fitting equation		R^2	K
Zero order $Q_t = Q_0 + K_0t$	pH 5	$y = 0.905x + 24.215$	0.9411	$k_0 = 0.905$
	pH 7	$y = 0.5737x + 15.05$	0.9305	$k_0 = 0.5737$
First order $\mathrm{Log}\, Q_t = \mathrm{Log}\, Q_0 - K_t/2.303$	pH 5	$y = 0.0085x + 1.3977$	0.7798	$k_1 = 0.0085$
	pH 7	$y = 0.0088x + 1.1845$	0.7289	$k_1 = 0.0088$
Higuchi $Q = K_H t^{1/2}$	pH 5	$y = 5.9345x + 0.9491$ $R^2 = 0.9849$	0.9849	$k_H = 5.9345$
	pH 7	$y = 5.4391x - 4.0918$	0.9905	$k_H = 5.4391$
Korsmeyer–Peppas model	pH 5	$y = 0.3617x - 0.7101$	0.9411	$K = 0.195$ $n = 0.3617$
	pH 7.4	$y = 0.3842x - 0.7281$	0.9573	$K = 0.187$ $n = 0.384$
Hixon–crowel $W_0^{1/3} - W_t^{1/3} = K_{HC} \times t$	pH 5	$y = -0.3017x + 25.262$	0.9411	$k_{HC} = 0.3017$
	pH 7.4	$y = -0.1912x + 28.317$	0.9344	$k_{HC} = 0.1912$

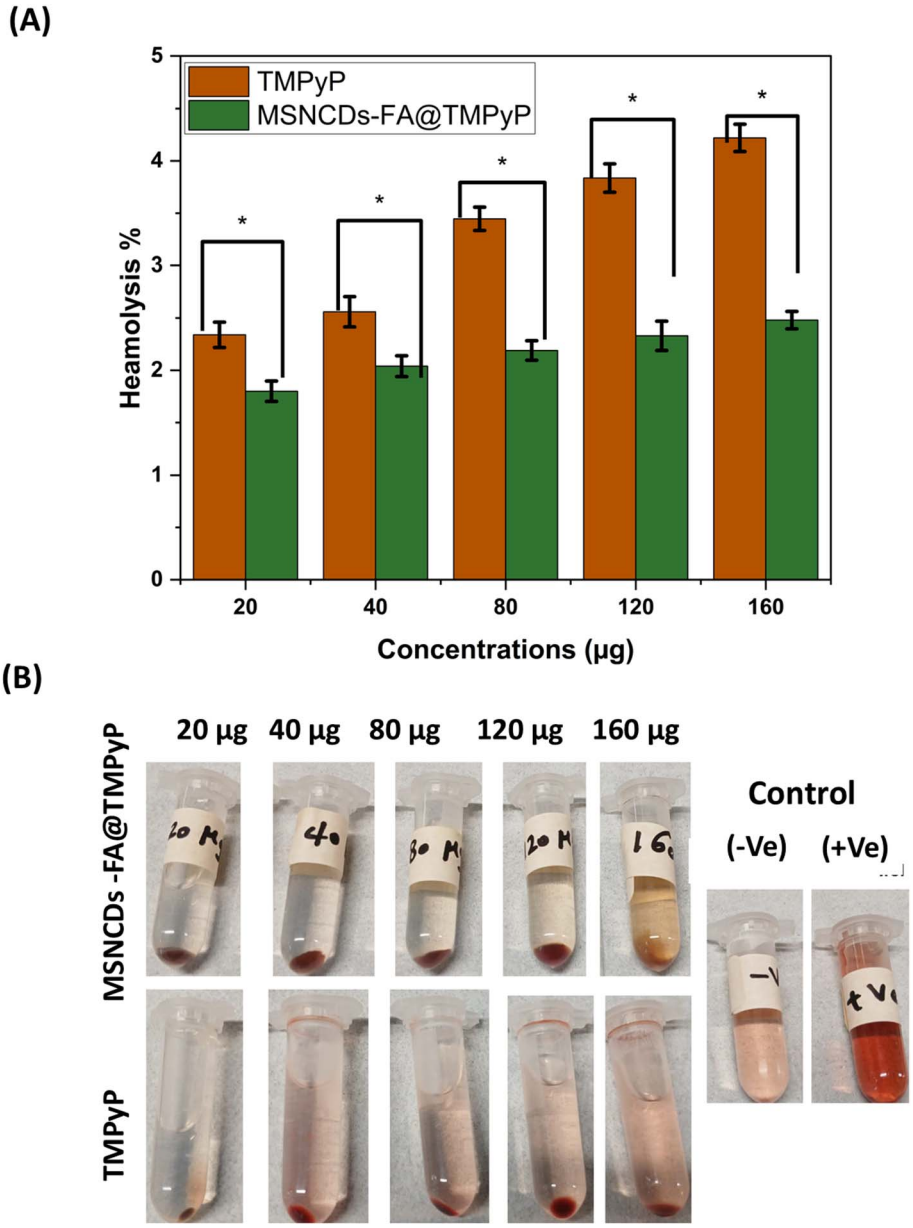

Fig. 6 (A) Hemolysis rate %, of RBCs from mouse treated by the synthesized MSNCDs, and MSNCDs-FA@TMPyP. (B) The Photographs of hemolytic activity assay (*$p < 0.05$).

release of TMPyP is primarily governed by diffusion-controlled kinetics.

The physical properties of the silica shell establish a rigid, porous matrix that facilitates the diffusion of the drug into the surrounding medium, aligning with this outcome.[70] The Korsmeyer–Peppas model demonstrated a good fit with release exponents of $n = 0.3617$ and $n = 0.384$, both of which are below the 0.45 threshold ($R^2 = 0.9696$ for pH 5 and $R^2 = 0.957$ for pH 7.4). This value corroborates the Higuchi interpretation, indicating that the release mechanism is predominantly governed by Fickian diffusion.[71] The system is appropriate for controlled drug delivery applications requiring sustained, diffusion-driven release.

Hemolysis test analysis

Hemocompatibility of TMPyP and the MSNCDs delivery system was evaluated using human red blood cell hemolysis assays (Fig. 6). At the maximum tested concentration of 160 μg mL^{-1}, free TMPyP exhibited a hemolysis rate below 5%, indicating the photosensitizer is intrinsically non-hemolytic and safe for blood-contact applications in the dark. Upon the incorporation of TMPyP into the MSNCD composite, the hemolysis rate further decreased to 2.48% at the same concentration. This reduction is attributed to the encapsulation of TMPyP within the MSNCD matrix, which limits direct interaction with erythrocyte membranes. Consequently, MSNCDs appear to enhance hemocompatibility by shielding the cationic TMPyP from

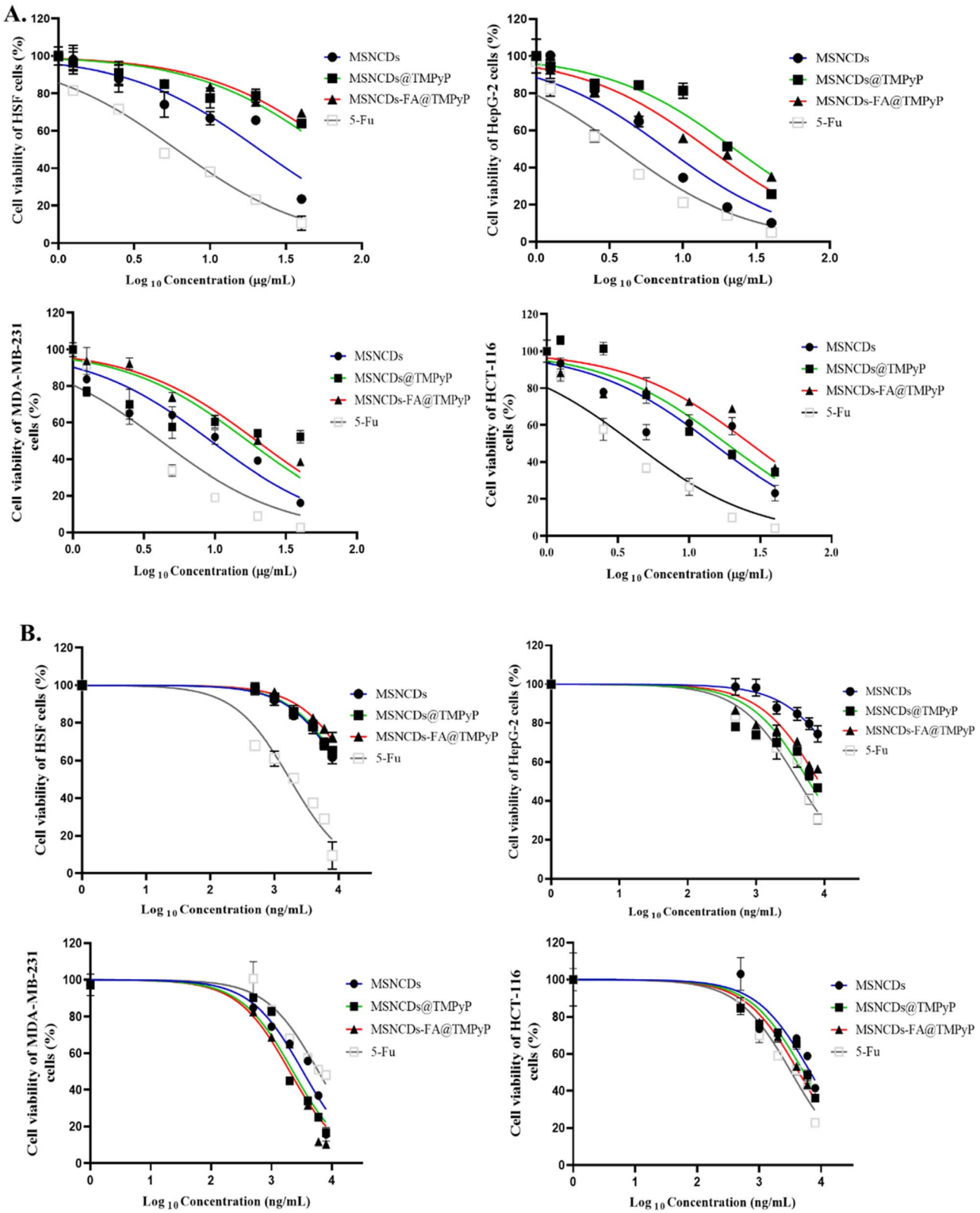

Fig. 7 Cytotoxic effects of the tested compounds on normal and cancerous cell lines. Dose-response curves show the percentage of cell viability in HSF (normal fibroblast), HepG-2 (liver cancer), MDA-MB-231 (breast cancer), and HCT-116 (colon cancer) cell lines following a 48-hour treatment. Viability was determined using the MTT assay. (A) Shows the cytotoxic effects under standard dark conditions, while (B) shows the effect following light irradiation. Data are presented as mean ± standard deviation (SD) of three independent experiments.

electrostatic interactions with negatively charged red blood cell surfaces.[72]

Assessment of *in vitro* cytotoxic effects

The anticancer potential of the tested compounds MSNCD, MSNCDs @TMPyP, and MSNCDs-FA@TMPyP was evaluated against three human cancer cell lines (MDA-MB-231, HepG-2, and HCT-116) and compared to the normal fibroblast cell line, HSF, to determine their therapeutic selectivity. The standard chemotherapeutic agent 5-FU was included as a reference. Cell viability was assessed *via* MTT assay after 48 hours of treatment, both under standard dark conditions and following photo-irradiation to evaluate photodynamic efficacy. Our findings revealed a clear dose-dependent cytotoxic effect for all compounds (Fig. 7A and B), with a notable difference in sensitivity among the cancer cell lines. In dark conditions, MSNCDs showed moderate toxicity to normal cells (CC_{50} = 21.17 μg mL^{-1}), the addition of TMPyP and folic acid significantly increased the CC_{50} to ~60–69 μg mL^{-1}, indicating a more favorable safety profile (Table 2). Probably attributable to the intrinsic cytotoxic properties of carbon dots derived from 5-fluorouracil.[73] Subsequent functionalization with TMPyP and folic acid significantly reduced the basal toxicity, increasing the CC_{50} values to approximately 60–69 μg mL^{-1}. This enhancement suggests that surface modification improves therapeutic targeting and contributes to a better safety profile, likely by decreasing nonspecific uptake in normal cells.[74]

The most selective compound in the dark was the targeted MSNCDs-FA@TMPyP, which showed potent activity against the HepG-2 cells (SI = 4.60). The true therapeutic potential of our system was realized upon activation with light. As hypothesized, the photodynamic effect dramatically increased the potency of the TMPyP-containing compounds (Table 3). This was most evident in the MDA-MB-231 breast cancer cells, which emerged as the most sensitive cell line to our photodynamic therapy. The potency of our modified compound, MSNCD-FA@TMPyP, against MDA-MB-231 cells increased nearly 9-fold, with its IC_{50} value increased from 19.69 μg mL^{-1} in the dark to just 2.31 μg mL^{-1} under light. Importantly, this increase in potency was accompanied by a remarkable increase in selectivity. The selectivity index of MSNCDs-FA@TMPyP against MDA-MB-231 cells surged to 8.44 upon irradiation, demonstrating a highly specific and powerful killing of triple negative breast cancer cell line while sparing normal tissue. The differences seen in selectivity index (SI) for the various cancer cell lines studied may be ascribed to a combination of biological and physicochemical factors. MDA-MB-231 breast cancer cells are known to overexpress folate receptor (FR-α), and to a much greater extent than either HepG2 or HCT-116 cells.[75,76] Since our MSNCDs-FA@TMPyP nanoplatform is functionalized with folic acid, it will preferentially accumulate in FR-rich cells through receptor-mediated endocytosis and, consequently, higher uptake and photodynamic response. HepG2 and HCT-116 cells, having a lower degree of folate receptor expression, will lead to reduced internalization of the nano formulation and, therefore, lower therapeutic efficacy and SI.[77,78]

In addition, the intracellular environment and redox status are different for cell lines. MDA-MB-231 cells will tend to have higher levels of metabolic activity and greater sensitivity to ROS, which combine to enhance photodynamic and chemotherapeutic cytotoxicity of the TMPyP-loaded system under irradiation.[79] Liver and colon cells are characterized by elevated antioxidant defenses and greater mechanisms for drug efflux which can often counterbalance ROS-mediated damage and reduce the effective intracellular accumulation of drug, leading to lower SI values.[80] This highlights a successful therapeutic strategy where active targeting *via* folic acid and an activatable photodynamic payload work in synergy to achieve highly selective cancer cell destruction.

Table 2 Cytotoxic activity of the synthesized derivatives under dark conditions against HepG-2, MDA-MB-231, and HCT-116 cancer cell lines, compared to normal human skin fibroblast cells (HSF), expressed as IC_{50} (μg mL^{-1}) and selectivity index (SI) values

	HSF	HepG-2		MDA-MB-231		HCT-116	
Sample code	CC_{50}	IC_{50}	SI	IC_{50}	SI	IC_{50}	SI
MSNCDs	21.17 ± 2.61	7.762 ± 0.91	2.73	9.34 ± 1.425	2.27	14.61 ± 2.32	1.45
MSNCDs@TMPyP	59.89 ± 3.43	22.46 ± 2.32	2.67	17.02 ± 4.53	3.52	18.25 ± 1.95	3.28
MSNCDs-FA@TMPyP	69.05 ± 4.45	19.01 ± 1.38	3.63	19.69 ± 6.44	3.51	26.77 ± 3.59	2.58
5-Fu	6.030 ± 0.48	3.812 ± 0.39	1.58	4.159 ± 0.57	1.45	4.09 ± 0.50	1.47

Table 3 Cytotoxic activity of the synthesized derivatives under light conditions against HepG-2, MDA-MB-231, and HCT-116 cancer cell lines, compared to normal human skin fibroblast cells (HSF), expressed as IC_{50} (μg mL^{-1}) and selectivity index (SI) values

	HSF	HepG-2		MDA-MB-231		HCT-116	
Sample code	CC_{50}	IC_{50}	SI	IC_{50}	SI	IC_{50}	SI
MSNCDs	13.08 ± 2.65	22.687 ± 4.63	0.577	3.567 ± 0.833	3.667	6.656 ± 0.636	1.965
MSNCD@TMPyP	14.037 ± 4.66	5.952 ± 1.64	2.358	2.446 ± 0.942	5.739	5.244 ± 0.734	2.677
MSNCDs-FA@TMPyP	19.491 ± 4.93	8.357 ± 1.68	2.332	2.309 ± 0.568	8.441	4.364 ± 0.933	4.466
5-Fu	5.22 ± 0.64	4.178 ± 1.37	1.249	4.026 ± 0.339	1.296	3.302 ± 1.69	1.580

To visually confirm the cytotoxic effects observed in the MTT assay, we examined the morphology of MDA-MB-231 cells—MDA-MB-231 is the most responsive cell line in the study—after a 48-hour treatment with the IC_{50} concentration of each compound. The bright-field microscopy images are presented in Fig. 8A. Untreated control cells displayed a healthy, confluent monolayer with a well-defined spindle-like morphology characteristic of MDA-MB-231 cell line. In contrast, cells treated with all tested compound, particularly MSNCD@TMPyP and MSNCD-FA@TMPyP, exhibited profound morphological changes. These included cell shrinkages, rounding, detachment from the plate surface, and the formation of apoptotic bodies, all hallmark indicators of significant cellular stress and cell death. The observed low-level ROS in the dark is likely due to the intrinsic redox activity of the TMPyP photosensitizer and potential residual electron transfer from the carbon dot core or silica matrix. Nonetheless, the baseline ROS levels were maintained within a moderate range, indicating a minimal risk of off-target oxidative stress under physiological conditions in the absence of light activation.

A key mechanism of photodynamic therapy is the generation of cytotoxic ROS. To investigate this, we used fluorescence microscopy to detect intracellular ROS levels in MDA-MB-231 cells following treatment (Fig. 8B). The control cells and those treated with the base MSNCDs showed minimal background fluorescence, indicating low endogenous ROS levels. However,

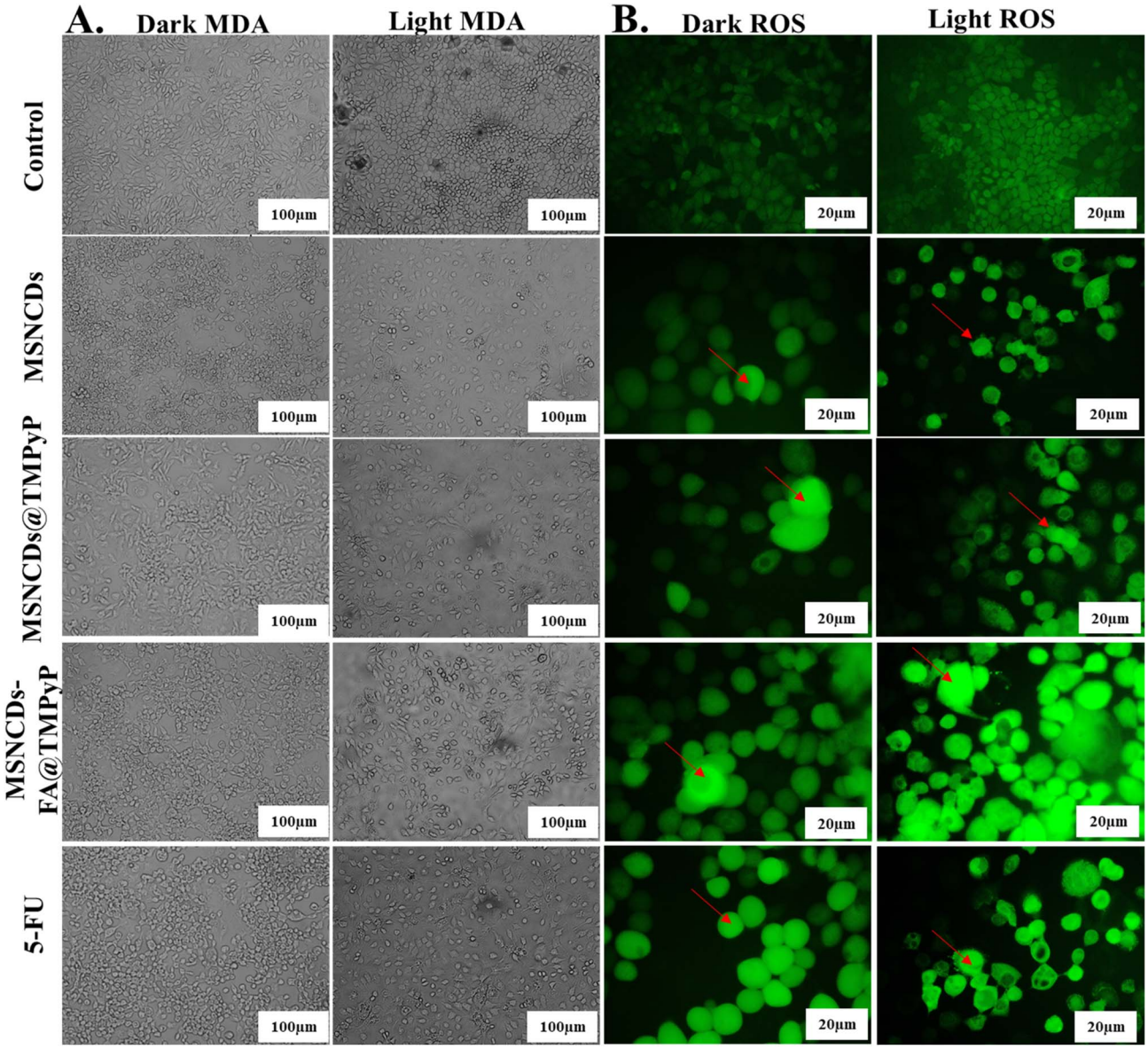

Fig. 8 (A) Bright-field microscopy images showing morphological changes in treated MDA cells under dark and light conditions, compared with untreated control cells. (B) Fluorescence microscopy images detecting intracellular reactive oxygen species (ROS) using the DCFH-DA probe. Cells were treated under standard dark conditions or following photo-irradiation (light). Increased green fluorescence (indicated by red arrows) signifies a high level of ROS. 5-Fluorouracil (5-FU) was included as a reference drug. Representative images of cells treated for 48 hours with the IC_{50} concentration of each compound.

a dramatic increase in green fluorescence was observed in cells treated with the TMPyP-loaded compounds, MSNCDs@TMPyP and MSNCDs-FA@TMPyP. This effect was slightly evident even in dark conditions, suggesting that the compounds themselves may induce some oxidative stress. As hypothesized, the ROS generation was massively amplified upon photo-irradiation. The most intense fluorescent signal was observed in cells treated with modified compound, MSNCDs-FA@TMPyP, under light. This indicates that the significant phototoxicity of the targeted and modified compound is directly promoted by the light-induced generation of elevated levels of intracellular ROS.

The increased production of reactive oxygen species (ROS) upon light exposure is directly associated with the rise in cytotoxicity observed in cancer cells, thereby reinforcing the role of ROS-mediated apoptosis as a key mechanism of cell death in photodynamic therapy. The inclusion of folic acid in MSNCDs-TMPyP-FA may facilitate increased intracellular uptake in folate receptor-positive cancer cells, which could enhance localized ROS production and improve therapeutic efficacy.

Furthermore, the apoptosis-mediated anticancer effect of the modified MSNCDs-FA@TMPyP nanoplatform at IC_{50} concentrations under dark and light conditions was evaluated by Annexin V-FITC/PI flow cytometry in MDA-MB-231 cells, as illustrated in Fig. 9A and B. According to established Annexin V/PI staining criteria, viable cells are Annexin V^-/PI^-, early apoptotic cells are Annexin V^+/PI^-, late apoptotic or secondary

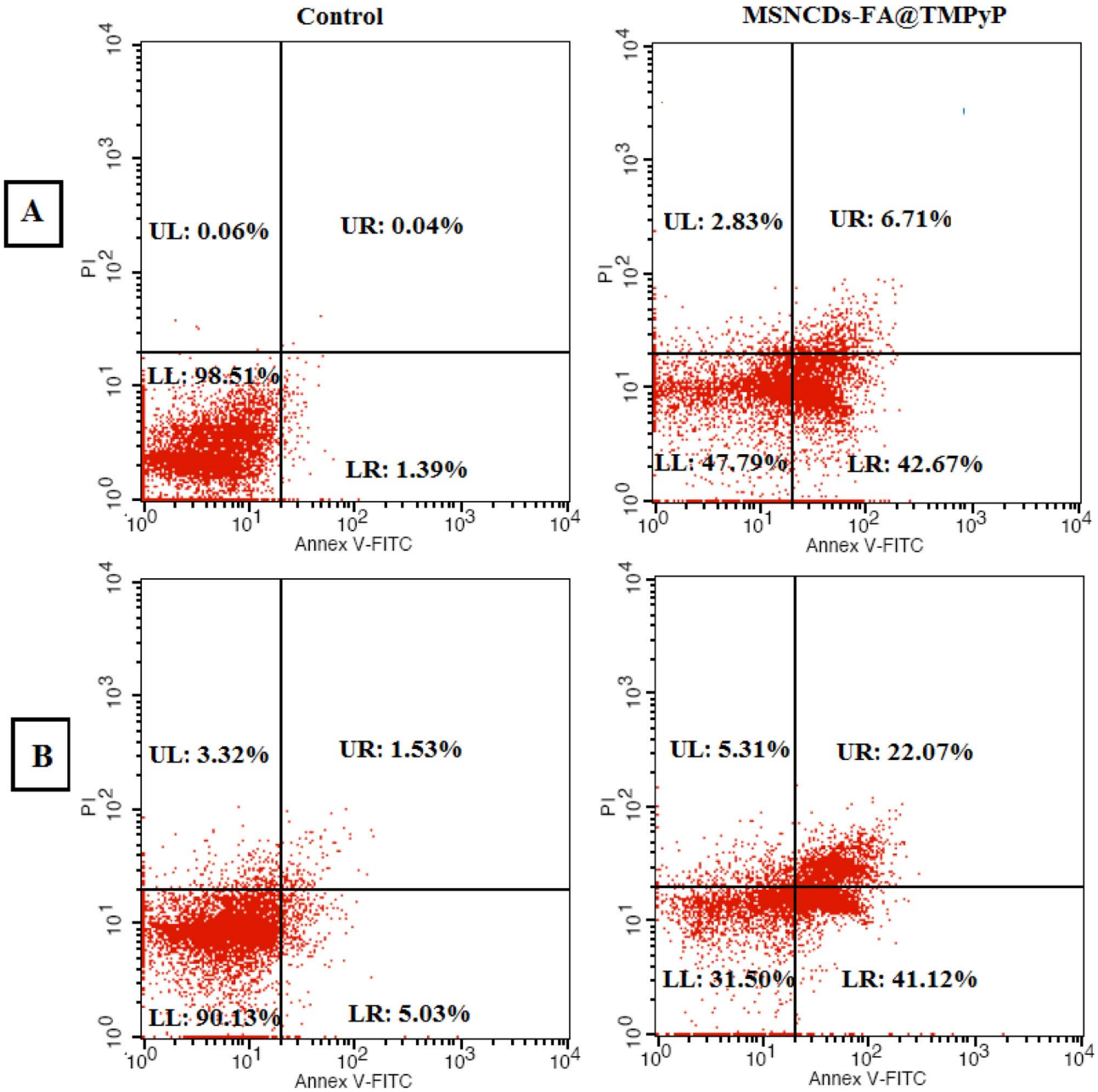

Fig. 9 Verification analysis of the apoptotic and necrotic effects of MSNCDs-FA@TMPyP compound in the treated and untreated (control) MDA-MB-231 cells using flow cytometric analysis of Annexin V/PI-stained at IC_{50} concentration under both dark (A) and light (B) conditions.

necrotic cells are Annexin V^+/PI^+, and primary necrotic cells are Annexin V^-/PI^+. Untreated control cells showed a predominantly viable population, with 98.51% and 90.13% viable cells under dark and light conditions, respectively, indicating minimal basal apoptosis or necrosis. Following treatment with MSNCDs-FA@TMPyP in the dark (Fig. 9A), a marked induction of apoptosis was observed, characterized by an increase in early apoptotic cells (42.67%) and a smaller late apoptotic population (6.71%), while primary necrosis remained minimal (2.83%). These results suggest that the cytotoxicity observed under dark conditions is mainly driven by apoptosis, likely due to the intrinsic chemotherapeutic activity of the fluorouracil-derived carbon dots and enhanced cellular uptake mediated by folic acid targeting. Upon light irradiation (Fig. 9B), the apoptotic response was significantly amplified. Early apoptotic cells accounted for 41.12%, while late apoptotic/secondary necrotic cells increased markedly to 22.07%, accompanied by a modest rise in primary necrosis (5.31%). The pronounced shift from early to late apoptosis under light exposure indicates photo-induced progression of programmed cell death, consistent with enhanced ROS generation following TMPyP photoactivation.

The predominance of apoptosis over primary necrosis under both dark and light conditions indicates that the MSNCDs-FA@TMPyP system mainly induces regulated cell death. The increase in late apoptotic cells following irradiation is likely due to ROS-mediated mitochondrial dysfunction and membrane damage, in agreement with the elevated ROS levels measured independently. Notably, the low proportion of necrotic cells is beneficial, as it is associated with a reduced risk of early inflammatory responses after localized treatment. This effect is further supported by folate targeting, which enhances selective accumulation of the photosensitizer and confines ROS generation to tumor cells rather than surrounding normal tissues.

One of the primary goals of cancer therapy is to induce apoptosis, or programmed cell death, in cancer cells. This process is driven by a family of enzymes called caspases, which act in a cascade to dismantle the cell.[81,82] We looked at the activity of two main caspases in this process: caspase-9, the initiator of the intrinsic (mitochondrial) pathway, and caspase-

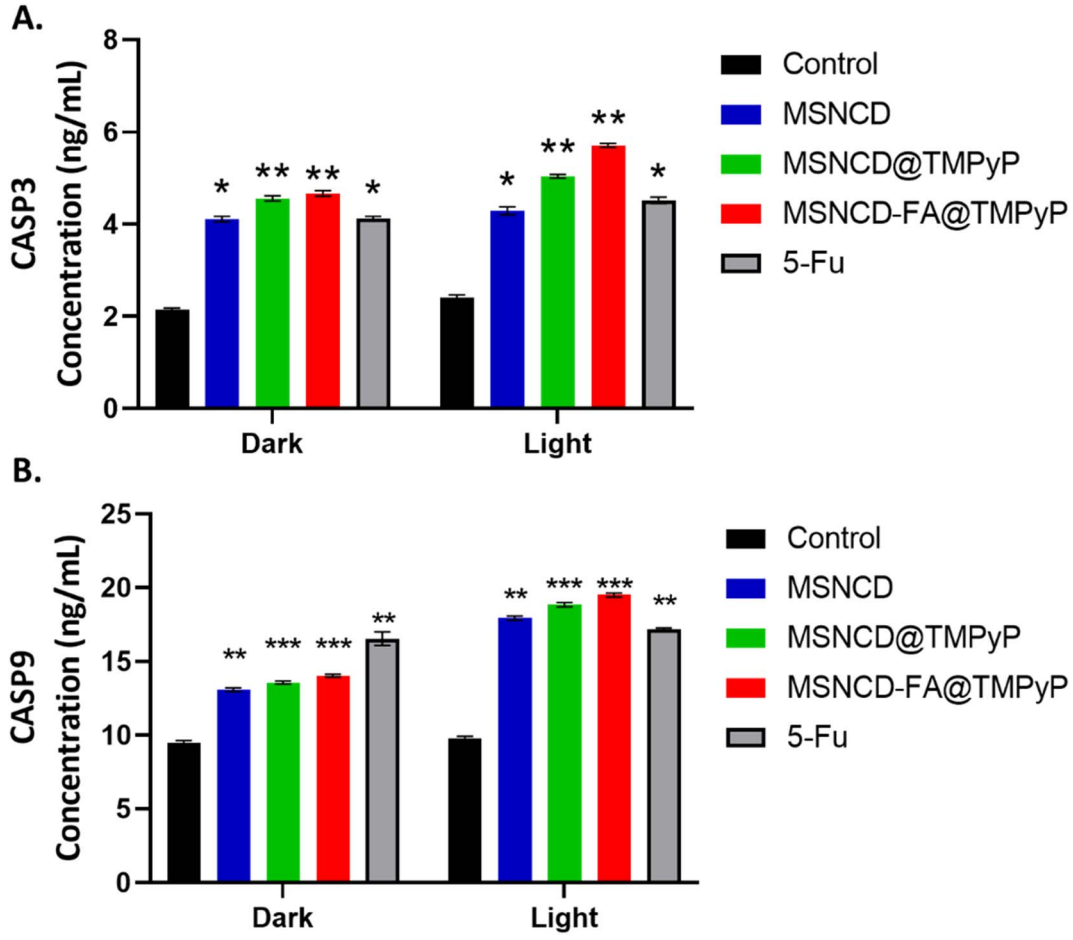

Fig. 10 Induction of apoptosis in MDA-MB-231 cells. The intracellular concentration (ng mL^{-1}) of (A) caspase-3, and (B) caspase-9, was quantified using ELISA following a 48-hour treatment with the IC_{50} concentration of each compound. Experiments were conducted under standard dark conditions and following photo-irradiation (light). Data represents the mean ± standard deviation (SD) from three independent experiments. Statistical analysis was performed using one-way ANOVA with Dunnett's post-hoc test. Significance compared to the control untreated group (*p < 0.05, **p < 0.01, ***p < 0.001).

3, the primary executioner caspase. Our results showed that all tested compounds induce apoptosis in MDA-MB-231 cells. We observed a significant increase in the activity of both caspase-3 (Fig. 10A) and caspase-9 (Fig. 10B) following a 48-hour treatment, both in dark and light-activated conditions. The most significant effect was seen with MSNCDs-FA@TMPyP, particularly upon activation by light, that confirms the cellular stress that trigger both extrinsic and intrinsic apoptotic pathway. The approximate two-fold increase in both caspase-3 and caspase-9 level, especially under light, directly explains the results we found in our cell viability assay. The potent activation of this apoptotic cascade is the suggested mechanism behind the low IC_{50} values and the extensive cell death we observed with the MTT test.

The photodynamic performance of MSNCDs-FA@TMPyP is comparable to other reported folate-targeted and carbon-dot-based photodynamic therapy (PDT) systems. Using our irradiation protocol, MSNCDs-FA@TMPyP significantly increased reactive oxygen species (ROS), leading to a total of ~63% apoptosis (41.12% early + 22.07% late) and only 5.31% necrosis. This impressive result was supported by the two-fold activation of caspase-9 and caspase-3 and low IC_{50} values (2.309 ± 0.568 at irradiation). Similar synergistic effects have been observed in other folate-targeted nanoplatforms that combine photothermal and photodynamic effects. For instance, the CDs-ICG-FA system achieved a high photothermal conversion efficiency (up to 34.3%) and substantial ROS production, which together induced significant MCF-7 cancer cell death through a synergistic photothermal/photodynamic process.[83]

To enhance photodynamic efficacy, a PEGylated mesoporous silica nanocarrier (MSN-PEG@Cur) containing curcumin was created to maximize dispersibility and cellular uptake. *In vitro* cytotoxicity studies using HeLa cells indicated that MSN-PEG@Cur demonstrated minimal toxicity in the absence of light, suggesting the nanoplatform is compatible with biological hosts in the dark. Light exposure, however, resulted in considerably higher cytotoxicity associated with a rapid increase in reactive oxygen species (ROS), compared to the lower ROS generation and cytotoxicity observed in the dark. The IC_{50} of MSN-PEG@Cur was determined to be 5.5 μg mL^{-1} *versus* free Cur IC_{50} of 22.9 μg mL^{-1}, which suggests that mesoporous silica construction and subsequent PEGylation can enhance the efficacy of PDT.[84]

Conclusion

In this study, we developed a multifunctional nanoplatform (MSNCDs-FA@TMPyP) engineered for the targeted treatment of triple-negative breast cancer (TNBC). This innovative system integrates chemotherapy, site-specific delivery, and photodynamic therapy (PDT) into a single therapeutic vehicle. The platform features a mesoporous silica framework embedded with 5-fluorouracil-derived carbon dots, a design that simultaneously enhances biocompatibility and provides intrinsic therapeutic functionality. To ensure high tumor specificity, the system is functionalized with folic acid for receptor-mediated endocytosis and loaded with the photosensitizer TMPyP. Comprehensive characterization confirmed the structural integrity and safety of the platform; notably, hemolysis levels remained below 5%, signifying excellent hemocompatibility. *In vitro* evaluations against MDA-MB-231 cells demonstrated a remarkable 9-fold increase in cytotoxicity upon light activation, supported by a high selectivity index of 8.44. Mechanistic analysis revealed that light-induced reactive oxygen species (ROS) generation triggers caspase activation, leading to significant apoptosis. These results establish this light-activatable, targeted nanoplatform as a promising candidate for aggressive breast cancer therapy, warranting further preclinical investigation.

Ethical approval

All experiments involving human blood samples were conducted in accordance with national, international, and institutional ethical guidelines. Human red blood cells were sourced from Alpha Lab (Alexandria, Egypt), a licensed clinical facility. The study was approved by the institutional ethical committee, and informed consent was obtained from all participants prior to sample collection.

Conflicts of interest

The authors declare that they have no known competing financial interests or personal relationships that could have appeared to influence the work reported in this paper.

Data availability

The datasets generated and/or analyzed during the current study are available from the corresponding author on reasonable request.

Supplementary information (SI): characterization of material included photostability, DLS size distribution data, and kinetic release profiles at pH 5.0 and 7.4. See DOI: https://doi.org/10.1039/d5ra10048h.

Acknowledgements

This work is supported by the Science, Technology & Innovation Funding Authority (STDF) under grant number 46207.

References

1 T. O. Abodunrin, G. O. Eghareyba, F. D. Oweye, J. A. Omojola and O. S. Adeyemi, Metal Organic Frameworks in Photodynamic Therapy of Cancer: Functional Roles of Active Metal Centers, Integrated and Loaded Photosensitizers in the Framework, *Mater. Adv.*, 2025, **6**, 1554–1577.

2 R. R. Cheruku, J. Cacaccio, F. Durrani, W. A. Tabaczynski, R. Watson, A. Marko, R. Kumar, M. E. El-Khouly, S. Fukuzumi, J. R. Missert, R. Yao, M. Sajjad, D. Chandra, K. Guru and R. K Pande, Epidermal Growth Factor Receptor (EGFR) Targeted Multifunctional Photosensitizers

for Bladder Cancer Imaging (Fluorescence/PET) and Photodynamic Therapy (PDT), *J. Med. Chem.*, 2019, **52**, 2598–2617.

3 Q. Zhou, G. Huang, J. Si, Y. Wu, S. Jin, Y. Ji and Z. Ge, Potent covalent organic framework nanophotosensitizers with staggered type I/II motifs for photodynamic immunotherapy of hypoxic tumors, *ACS Nano*, 2024, **18**, 35671–35683.

4 M. Yang, Y. Kim, S.-Y. Youm, H. Jeongm, M. E. Shirbhatem, C. Uhm, G. Kim, K. T. Nam, S.-C. Cha, K. M. Kim and J. Yoon, Conversion of albumin into a BODIPY-like photosensitizer by a flick reaction, tumor accumulation and photodynamic therapy, *Biomaterials*, 2025, **313**, 122792.

5 S. M. Costa, *et al.*, Localized cancer photodynamic therapy approach based on core–shell electrospun nanofibers, *Mater. Adv.*, 2024, **5**, 6489–6500.

6 L. M. O. Lourenço, *et al.*, Thioglycerol-porphyrin, -chlorin, and -phthalocyanine derivatives for photodynamic therapy of UM-UC-3 bladder cancer cells, *J. Photochem. Photobiol., A*, 2023, **442**, 114768.

7 S. Sivaselvam, M. Veena and N. Ponpandian, Metal organic framework based photodynamic therapy for cancer treatment, in *Nanophototherapy*, Elsevier, 2025. pp. 419–434.

8 A. Mokhtar, T. Mohamed, A. O. Eigza and M. E. El-Khouly, Water-soluble porphyrin-mediated enhanced photodynamic and chemotherapy employing doxorubicin for breast cancer, *Laser Med. Sci.*, 2025, **40**, 241.

9 A. Imanparast, *et al.*, A preclinical design approach for translation of biohybrid photosensitive nanoplatform for photodynamic therapy of breast cancer, *J. Controlled Release*, 2025, **378**, 543–558.

10 B. Güleryüz, A. Işık and M. Gülsoy, Synergistic effect of mesoporous silica nanocarrier-assisted photodynamic therapy and anticancer agent activity on lung cancer cells, *Laser Med. Sci.*, 2024, **39**, 91.

11 X. Liang, *et al.*, Mesoporous silica coated spicules for photodynamic therapy of metastatic melanoma, *J. Nanobiotechnol.*, 2024, **22**, 179.

12 Y. Cheng, *et al.*, Variability and improvement of optical and antimicrobial performances for CQDs/mesoporous SiO_2/AgNPs composites via in situ synthesis, *Green Process. Synth.*, 2021, **10**, 403–411.

13 X. Li, *et al.*, Dual-responsive mesoporous silica nanoparticles coated with carbon dots and polymers for drug encapsulation and delivery, *Nanomedicine*, 2020, **15**, 2447–2458.

14 P. Pongchaikul, *et al.*, Nanostructured N/S doped carbon dots/mesoporous silica nanoparticles and PVA composite hydrogel fabrication for anti-microbial and anti-biofilm application, *Int. J. Pharm.:X*, 2023, **6**, 100209.

15 O. Mkhari, T. D. Ntuli, N. J. Coville, E. N. Nxumalo and M. S. Maubane-Nkadimeng, A comparison of fluorescent N-doped carbon dots supported on the surface of hollow and solid carbon spheres, and solid silica spheres, *Diamond Relat. Mater.*, 2021, **118**, 108500.

16 B. Tian, s. Liu, C. Yu, S. Liu, S. Dong, L. Feng, N. Hu and P. Yang, A Metal-Free Mesoporous Carbon Dots/Silica Hybrid Type I Photosensitizer with Enzyme-Activity for Synergistic Treatment of Hypoxic Tumor, *Adv. Funct. Mater.*, 2023, **33**, 2300818.

17 H. Kirla, *et al.*, One-pot synthesis and covalent conjugation of methylene blue in mesoporous silica nanoparticles–a platform for enhanced photodynamic therapy, *Colloids Surf., B*, 2025, **245**, 114195.

18 K. Chen, Y. Tao, X. An, X. Jiang, D. Li, Q. Xu, X. Zhang, J. Zhang, L. Xu and M. Gao, H_2O_2 promotes photodynamic efficacy of TMPyP4 against ovarian cancer in vitro by downregulating HIF-1α expression, *Biomed. Pharmacother.*, 2024, **177**, 117110.

19 Y. Liu, Y. Tao, X. A, X. Jiang, D. Li, Q. Xu, X. Zhang, J. Zhang, L. Xu and M. Gao, High dispersibility ratiometric fluorescence sensor designed by functionalized mesoporous silica nanopraticles for sensing and imaging of hydrogen peroxide, *Colloids Surf., A*, 2024, **683**, 132971.

20 C. Olla and C. Carbonaro, The void side of silica: Surveying optical properties and applications of mesoporous silica, *J. Phys.: Condens. Matter*, 2024, **36**, 253002.

21 L. R. Carobeli, A. B. C. Sabtos, L. B. M. Martins, E. Damke and M. E. L. Consolaro, Recent advances in photodynamic therapy combined with chemotherapy for cervical cancer: a systematic review, *Expert Rev. Anticancer Ther.*, 2024, **24**, 263–282.

22 X. Zheng, X. Wang, J. Chen, J. Wu, M. Zhou, R. Xia, W. Wang, X. Zheng and Z. Xie, Recent progress of porphyrin metal-organic frameworks for combined photodynamic therapy and hypoxia-activated chemotherapy, *Chem. Commun.*, 2024, **60**, 13641–13652.

23 Z. Tu, Y. Wan, J. Ge, C.-C. Li, T. Liang and Z. Li, NIR-IIb-triggered photodynamic therapy combined with chemotherapy platform based on rare-earth-doped nanoparticles, *Rare Met.*, 2024, **43**, 3220–3231.

24 L. He, X. Nan, T. Wang and P. Bai, Glutathione and pH Serial Responsive Functional Mesoporous Silica Nanoparticles for Drug Delivery, *Micro Nano Lett.*, 2020, **15**, 291–295.

25 I. Ahmad, S. Ahmed, Z. Anwar, M. A. Sheraz and M. Sikorski, Photostability and Photostabilization of Drugs and Drug Products, *Int. J. Photoenergy*, 2016, 8135608.

26 G. T. McMullon, *et al.*, Synthesis and Characterization of Folsic Acid-Conjugated Terbium Complexes as Luminescent Probes for Targeting Folate Receptor-Expressing Cells, *J. Med. Chem.*, 2024, **67**, 14062–14076.

27 A. Ardhi and M. Schreiner, Evaluation of extraction and entrapment efficiency of black seed oil-containing emulsion as a delivery system for thymoquinone, *J. Food Meas. Char.*, 2024, **18**, 393–401.

28 P. Acedo, J. C. Stockert, M. Canete and A. Villanueva, Two combined photosensitizers: a goal for more effective photodynamic therapy of cancer, *Cell Death Dis.*, 2014, **5**, e1122.

29 M. Czarnecka-Czapczyńska, D. Aebisher, P. Oleś, B. Sosna, M. Krupka-Olek, K. Dynarowicz, W. Latos, G. Cieślar and A. Kawczyk-Krupka, The role of photodynamic therapy in breast cancer – A review of in vitro research, *Biomed. Pharmacother.*, 2021, **144**, 112342.

30 E. Serag, E. M. Fakharany, S. Hammad and M. E. El-Khouly, Metal–organic framework MIL-101(Fe) functionalized with folic acid as a multifunctional nanocarrier for targeted chemotherapy–photodynamic therapy, *Biomater. Sci.*, 2025, **13**, 2351–2367.
31 E. Serag, S. A. Abdel Gaber and M. E. El-Khouly, Perylene tetracarboxylic acid-folate conjugated carbon quantum dots for targeted photodynamic therapy of prostate cancer, *Bioorg. Chem.*, 2025, **163**, 108631.
32 S. H. El-Moslamy, *et al.*, Facile phyto-mediated synthesis of ternary CuO/Mn_3O_4/ZnO nanocomposite using Nigella Sativa seeds extract: characterization,antimicrobial, and biomedical evaluations, *Sci. Rep.*, 2025, **15**, 16139.
33 P. Sivolapov, O. Myronyuk and D. Baklan, Synthesis of Stober silica nanoparticles in solvent environments with different Hansen solubility parameters, *Inorg. Chem. Commun.*, 2022, **143**, 109769.
34 D. Dorairaj, *et al.*, Green synthesis and characterization of UKMRC-8 rice husk-derived mesoporous silica nanoparticle for agricultural application, *Sci. Rep.*, 2022, **12**, 20162.
35 N. Sharma, I. Sharma and M. K. Bera, Microwave-Assisted Green Synthesis of Carbon Quantum Dots Derived from Calotropis Gigantea as a Fluorescent Probe for Bioimaging, *J. Fluoresc.*, 2022, **32**, 1–11.
36 M. Schneider, *et al.*, Synthesis and characterization of silica-based nanofluids for enhanced oil recovery, *J. Mater. Res. Technol.*, 2023, **24**, 4143–4152.
37 M. Skorupska, *et al.*, The Improvement of Energy Storage Performance by Sucrose-Derived Carbon Foams via Incorporating Nitrogen Atoms, *Nanomaterials*, 2021, **11**, 760.
38 A. Cassidy, *et al.*, Adsorption of 5-Fluorouracil on Au(111) and Cu(111) surfaces, *AIP Adv.*, 2019, **9**, 085318.
39 R. Ellerbrock, M. Stein and J. Schaller, Comparing amorphous silica, short-range-ordered silicates and silicic acid species by FTIR, *Sci. Rep.*, 2022, **12**, 11708.
40 Fourier Transform Infrared and Raman Characterization of Silica-Based Materials, *Applications of Malecular Spectroscopy to Current Research in the Chemical and Biological Sciences*, ed. L. Capeletti and J. Zimnoch, InterchOpen, 2016.
41 C. Hu, *et al.*, One-step preparation of nitrogen-doped graphene quantum dots from oxidized debris of graphene oxide, *J. Mater. Chem. B*, 2012, **1**, 39–42.
42 D. Predoi, *et al.*, Properties of Basil and Lavender Essential Oils Adsorbed on the Surface of Hydroxyapatite, *Materials*, 2018, **11**, 652.
43 F. Dai, *et al.*, Infrared Spectrum Characteristics and Quantification of OH Groups in Coal, *ACS Omega*, 2023, **8**, 17064–17076.
44 S. Darmakkolla, H. Tran, A. Gupta and S. B. Rananavare, A method to derivatize surface silanol groups to Si-alkyl groups in carbon-doped silicon oxides, *RSC Adv.*, 2016, **6**, 93219–93230.
45 P. Chandel, S. Sharma, I. Mohiuddin and S. Bhogal, Mesoporous silica-encapsulated nitrogen-doped fluorescent carbon dots modified polydopamine composites for monitoring non-steroidal anti-inflammatory drugs, *Microchem. J.*, 2024, **204**, 111000.
46 A. Čeklovský, *et al.*, Spectral properties of TMPyP intercalated in thin films of layered silicates, *J. Colloid Interface Sci.*, 2008, **324**, 240–245.
47 X. Zhang, *et al.*, Porphyrin Functionalized Carbon Quantum Dots for Enhanced Electrochemiluminescence and Sensitive Detection of Cu, *Molecules*, 2023, **28**, 1459.
48 M. Abdelaziz Youssef, *et al.*, In vitro release and cytotoxicity activity of 5-fluorouracil entrapped polycaprolactone nanoparticles, *Polym. Bull.*, 2022, **79**, 6645–6671.
49 A. Biradar, P. D. Sarvalkar, S. B. Teli, C. A. Pawar, P. S. Patil and N. R. Prasad, Photocatalytic degradation of dyes using one-step synthesized silica nanoparticles, *Mater. Today: Proc.*, 2021, **43**, 2823–2838.
50 A. Habib, *et al.*, Kinetics and mechanism of formation of nickel(II)porphyrin and its interaction with DNA in aqueous medium, *J. Chem. Sci.*, 2021, **133**, 83.
51 A. Stallivieri, *et al.*, Folic acid conjugates with photosensitizers for cancer targeting in photodynamic therapy: Synthesis and photophysical properties, *Bioorg. Med. Chem.*, 2017, **25**, 1–10.
52 L. Mkrtchyan, T. Seferyan, M. Parkhats, S. Lepeshkevisch, B. Dzhagarov, G. Shmavonyan, E. Tuchina, V. Tuchin and G. Gyulkhandanyan, The role of singlet oxygen and hydroxyl radical in the photobleaching of meso-substituted cationic pyridyl porphyrins in the presence of folic acid, *J. Innovative Opt. Health Sci.*, 2024, **17**, 2440002.
53 H. Shinoda, R. Higano, T. Oizumi, A. J. Nakamura, T. Kamijo, M. Takahashi, M. Nagaoka, Y. Sato and A. Yamaguchi, Albumin Hydrogel-Coated Mesoporous Silica Nanoparticle as a Carrier of Cationic Porphyrin and Ratiometric Fluorescence pH Sensor, *ACS Appl. Bio Mater.*, 2024, **7**, 1204–1213.
54 H. Cao, *et al.*, Stability of quercetin in DMEM and cell culture with A549 cells, *eFood*, 2022, **3**, e13.
55 J. Lim, *et al.*, Characterization of magnetic nanoparticle by dynamic light scattering, *Nanoscale Res. Lett.*, 2013, **8**, 381.
56 X. Zou, *et al.*, Porous silica nanoparticles capped with polyethylenimine/green carbon dots for pH/redox responsive drug release, *Inorg. Chem. Commun.*, 2020, 108340.
57 Y. Wang, *et al.*, Effects of surface modification and size on oral drug delivery of mesoporous silica formulation, *J. Colloid Interface Sci.*, 2018, **513**, 736–747.
58 S. Lee, Highly uniform silica nanoparticles with finely controlled sizes for enhancement of electro-responsive smart fluids, *J. Ind. Eng. Chem.*, 2019, **77**, 426–431.
59 J. Xu, *et al.*, Preparation of hollow nanoparticles with controllable diameter by one-step controlled etching of microporous silica particles using an ammonia-based etchant, *Colloids Surf., A*, 2020, **592**, 124579.
60 M. Meier, *et al.*, Synthesis of nanometric silica particles via a modified Stöber synthesis route, *Colloids Surf., A*, 2018, **538**, 559–564.
61 I. E. Moujarrad, *et al.*, Size-tuning of hollow periodic mesoporous organosilica nanoparticles (HPMO-NPs) using

a dual templating strategy, *J. Sol-Gel Sci. Technol.*, 2023, **107**, 302–311.

62 R. Prieto-Montero, *et al.*, Functionalization of Photosensitized Silica Nanoparticles for Advanced Photodynamic Therapy of Cancer, *Int. J. Mol. Sci.*, 2021, **22**, 6618.

63 S. Li, *et al.*, Multifunctional mesoporous silica nanoplatform based on silicon nanoparticles for targeted two-photon-excited fluorescence imaging-guided chemo/photodynamic synergetic therapy in vitro, *Talanta*, 2020, **209**, 120552.

64 X. Liu, *et al.*, Folic acid-conjugated hollow mesoporous silica/CuS nanocomposites as a difunctional nanoplatform for targeted chemo-photothermal therapy of cancer cells, *J. Mater. Chem. B*, 2014, **2**, 5358–5367.

65 Y. Jin, W. Tang, J. Wang, F. Ren, Z. Chen, Z. Sun and P. -Gang Ren, Construction of biomass derived carbon quantum dots modified TiO_2 photocatalysts with superior photocatalytic activity for MB degradation, *J. Alloys Compd.*, 2023, **932**, 167627.

66 M. Wang, *et al.*, Monolayer porphyrin assembled SPSf/PES membrane reactor for degradation of dyes under visible light irradiation coupling with continuous filtration, *J. Taiwan Inst. Chem. Eng.*, 2020, **109**, 62–70.

67 S. Saita and H. Kawasaki, Carbon nanodots with a controlled N structure by a solvothermal method for generation of reactive oxygen species under visible light, *Luminescence*, 2023, **38**(2), 127–135.

68 Y. Zhang, Q. Jia, F. Nan, J. Wang, K. Liang, J. Li, X. Xue, H. Ren, W. Liu, J. Ge and P. Wang, Carbon dots nanophotosensitizers with tunable reactive oxygen species generation for mitochondrion-targeted type I/II photodynamic therapy, *Biomaterials*, 2023, **293**, 121953.

69 Z. Wang, X. Deng, J. Ding, W. Zhou, X. Zheng and G. Tang, Mechanisms of drug release in pH-sensitive micelles for tumour targeted drug delivery system: A review, *Int. J. Pharm.*, 2018, **535**, 253–260.

70 Q. Tang, B. Yu, L. Gao, H. Cong, N. Song and C. Lu, Stimuli Responsive Nanoparticles for Controlled Anti-cancer Drug Release, *Curr. Med. Chem.*, 2018, **25**(16), 1837–1866.

71 G. Dolete, *et al.*, A Comparative Loading and Release Study of Vancomycin from a Green Mesoporous Silica, *Molecules*, 2022, **27**, 5589.

72 M. Fosca and J. Rau, Factors influencing the drug release from calcium phosphate cements, *Bioact. Mater.*, 2022, **7**, 341–363.

73 L. Li, *et al.*, The photosensitizer system based on cationic COF carrier with the loading tetraminoporphyrin and its combined antibacterial effect, *New J. Chem.*, 2024, **48**, 14155–14162.

74 Q. Zeng, *et al.*, Precursor-dependent structural diversity in luminescent carbonized polymer dots (CPDs): the nomenclature, *Light: Sci. Appl.*, 2021, **10**, 142.

75 S. Singh and K. Pal, Folic-acid adorned alginate-polydopamine modified paclitaxel/Zn-CuO nanocomplex for pH triggered drug release and synergistic antitumor efficacy, *Int. J. Biol. Macromol.*, 2023, **234**, 123602.

76 S. D. Weitman, R. H. Lark, L. R. Coney, D. W. Fort, V. Frasca, V. R. Zurawski and B. A. Kamen, Distribution of the folate receptor GP38 in normal and malignant cell lines and tissues, *Cancer Res.*, 1992, **52**, 3396–3401.

77 Y. Jing, L. Huang, Z. Dong, Z. Gong, B. Yu, D. Lin and J. Qu, Super-resolution imaging of folate receptor alpha on cell membranes using peptide-based probes, *Talanta*, 2023, **268**, 125286.

78 R. Wu, C. Linag, J. Zou, C. Li, Y. Yan, X. Hu and X. Ling, Detection of membrane receptors on per tumor cell by nonimmobilized cell capillary electrophoresis and a mathematic model, *Talanta*, 2021, **222**, 121425.

79 S. Ju, M. K. Singh, S. Han, J. Ranbhise, J. Ha, W. Choe, K.-S. Yoon, S. G. Yeo, S. S. Kim and I. Kang, Oxidative Stress and Cancer Therapy: Controlling Cancer Cells Using Reactive Oxygen Species, *Int. J. Mol. Sci.*, 2024, **25**, 12387.

80 R. Wang, L. Liang, M. Matsumoto, K. Iwata, A. Umemura and F. He, Reactive Oxygen Species and NRF2 Signaling, Friends or Foes in Cancer?, *Biomolecules*, 2023, **13**, 353.

81 P. Inthi, *et al.*, Anti-cancer effect and active phytochemicals of Houttuynia cordata thunb, against human breast cancer cells, *Asian Pac. J. Cancer Prev.*, 2023, **24**, 1265.

82 M. Y. Seo and K. Rhee, Caspase-mediated cleavage of the centrosomal proteins during apoptosis, *Cell Death Dis.*, 2018, **9**, 571.

83 M. Shaofang, Y. Zhang, Z. Zhu, D. Wang, J. Wang, W. Bian and X. Tang, Nucleolus-Targeting Carbon Dot Nanocomplexes for Combined Photodynamic/Photothermal Therapy, *Mol. Pharm.*, 2025, **22**, 958–971.

84 G. Kuang, Q. Zhang, S. He and Y. Liu, Curcumin-loaded PEGylated mesoporous silica nanoparticles for effective photodynamic therapy, *RSC Adv.*, 2020, **10**, 24624–24630.